

1     **Aseismic Fault Slip during a Shallow Normal-Faulting**  
2             **Seismic Swarm Constrained Using a**  
3             **Physically-Informed Geodetic Inversion Method**

4             **Yu Jiang<sup>1</sup>, Sergey V. Samsonov<sup>2</sup>, and Pablo J. González<sup>1,3</sup>**

5     <sup>1</sup>COMET, Dept. Earth, Ocean and Ecological Sciences, School of Environmental Sciences, University of  
6             Liverpool, Liverpool, L69 3BX, United Kingdom.

7     <sup>2</sup>Canada centre for Mapping and Earth Observation, Natural Resources Canada, 560 Rochester Street,  
8             Ottawa, ON K1S5K2, Canada.

9     <sup>3</sup>Department of Life and Earth Sciences, Instituto de Productos Naturales y Agrobiología (IPNA-CSIC),  
10             38206 La Laguna, Tenerife, Canary Islands, Spain.

11     **Key Points:**

- 12     • We invert for time-dependent fault slip distribution from geodetic data, based on  
13         a low dimensional model for elliptical slip distributions.
- 14     • Significant aseismic slip preceded the most energetic M4.6 event in the 2011 Hawthorne  
15         shallow seismic swarm.
- 16     • Average slip rates (lower bound) of this swarm and slow-slip phenomena are sim-  
17         ilar, implying a notable role of aseismic processes in swarms.

---

Corresponding author: Yu Jiang, [jiangyuinsar@gmail.com](mailto:jiangyuinsar@gmail.com)

18 **Abstract**

19 Improved imaging of the spatio-temporal growth of fault slip is crucial for understand-  
20 ing the driving mechanisms of earthquakes and faulting. This is especially critical to prop-  
21 erly evaluate the evolution of seismic swarms and earthquake precursory phenomena. Fault  
22 slip inversion is an ill-posed problem and hence regularisation is required to obtain sta-  
23 ble and interpretable solutions. An analysis of compiled finite fault slip models shows  
24 that slip distributions can be approximated with a generic elliptical shape, particularly  
25 well for  $M \leq 7.5$  events. Therefore, we introduce a new physically-informed regularisation  
26 to constrain the spatial pattern of slip distribution. Our approach adapts a crack model  
27 derived from mechanical laboratory experiments and allows for complex slipping pat-  
28 terns by stacking multiple cracks. The new inversion method successfully recovered dif-  
29 ferent simulated time-dependent patterns of slip propagation, i.e., crack-like and pulse-  
30 like ruptures, directly using wrapped satellite radar interferometry (InSAR) phase ob-  
31 servations. We find that the new method reduces model parameter space, and favours  
32 simpler interpretable spatio-temporal fault slip distributions. We apply the proposed method  
33 to the 2011 March-September normal-faulting seismic swarm at Hawthorne (Nevada, USA),  
34 by computing ENVISAT and RADARSAT-2 interferograms to estimate the spatio-temporal  
35 evolution of fault slip distribution. The results show that (1) aseismic slip might play  
36 a significant role during the initial stage, and (2) this shallow seismic swarm had slip rates  
37 consistent with those of slow earthquake processes. The proposed method will be use-  
38 ful in retrieving time-dependent fault slip evolution and is expected to be widely appli-  
39 cable to studying fault mechanics, particularly in slow earthquakes.

**Plain Language Summary**

41 A key earthquake science challenge is to understand when an instability on a fault  
42 will arrest or run away into a large rupture. However, the slip nucleation process seems  
43 not to produce seismic waves and hence remains hidden to most seismological methods.  
44 Geodetic methods, which can directly measure motions at earth's surface, offer a com-  
45plementary tool to improve our ability to map the fault slip. In this work, we expand  
46an experimentally observed crack model, and propose a new inversion method for find-  
47ing models of fault slip that can fit the observations of surface motions. The new method  
48greatly reduces computation complexity respecting previous state-of-the-art methods,  
49and is validated against synthetic experiments. We apply this new method to 2011 Hawthorne  
50earthquake swarm (Nevada, USA), and discovered an aseismic slow slip before seismic-  
51ity rate increased. That preparation stage was followed by a triggered larger slip on a  
52nearby fault, and after that, the seismicity and fault slip rate reduced rapidly. We ex-  
53pect that this new methodology will be applied to detect similar precursory aseismic slip  
54during long-lasting earthquake sequences, and allow us to retrieve detailed slip growth  
55in space and time, which ultimately will advance our understanding of the faulting me-  
56chanics.

## 1 Introduction

How fault slip nucleates, grows and eventually accelerates is a critical question to describe the driving mechanisms behind earthquakes and faulting phenomena. Our current understanding is consistent but cannot distinguish among various viable mechanisms to explain how fault slip initiates: dynamic triggering (Gomberg & Johnson, 2005), tidal triggering (Delorey et al., 2017), pore-pressure diffusion (Parotidis et al., 2003) or aseismic slip (Radiguet et al., 2016; Gualandi et al., 2017; Caballero et al., 2021). In particular, Gomberg (2018) summarised two leading hypotheses for earthquake nucleation. Ranging from a stochastic model in which each earthquake triggers subsequent ones in a cascade fashion, to an alternative that favours a deterministic view where slow-slip triggers and/or precedes the occurrence of a seismically dynamic rupture. Within the scope of increasing our capacity to distinguish between the earthquake nucleation models, a promising venue is to increase our ability to image how fault slip evolves in space and time. Although fault slip evolution is not necessarily the only cause of seismicity migrating, improvements in this direction may provide crucial data to examine hypotheses for earthquake nucleation mechanisms.

Fault slip imaging improvements are particularly desirable to estimate (seismic and aseismic) slip propagation parameters, such as slip rate, and gain deeper insights into the physics controlling regular earthquakes and slow-slip phenomena. Regular earthquakes are known to show peak and average slip rates of the order of 1 m/s and 0.1 m/s (Takenaka & Fujii, 2008). While slow-slip phenomena show much lower slip rates, e.g., Slow Slip Events (SSEs), fault creep, or slip related to fluid injection. For example, in the case of SSEs in subduction zones, the peak slip rates vary around 0.1~3 cm/day (Radiguet et al., 2011; Bletery & Nocquet, 2020; Rousset et al., 2019; Ozawa et al., 2019). In the case of the episodic creep event, the slip rates in continental faults are 0.5~3 cm/year (Schmidt et al., 2005; Jolivet et al., 2012; Hussain et al., 2016; Scott et al., 2020). In fluid injection experiments, the slip rates have been observed to be much higher, up to  $4 \times 10^{-3}$  mm/s (35 cm/day) (Guglielmi et al., 2015).

Hence, to evaluate (seismic and aseismic) fault slip characteristics, a better description of how fault slip propagates in space and time is necessary. Including complex propagation patterns of fault slip such as pulse-like and crack-like ruptures (Lambert et al., 2021; Marone & Richardson, 2006). Such patterns have been observed during regular

89 earthquakes but are also associated with slow-slip phenomena: with slow slip transients  
90 migrating further away from where they started along strike (or dip), or remain station-  
91 ary through time. Observations of some SSEs and "Episodic Tremor and Slip" (ETS)  
92 show pulse-like rupture characteristics with elongated slipping areas, e.g., the Cascadia  
93 subduction zone (Michel et al., 2019), and with along strike migration speeds of  $\sim 10$  km/day  
94 (Wech et al., 2009; Rousset et al., 2019). In contrast, slip propagation of meter-scale fluid  
95 injection experiments indicates stationary patterns: Bhattacharya and Viesca (2019) pro-  
96 posed a model in which the slip grows as an expanding ellipse, with the injection point  
97 as the slipping centre. The latter phenomenon is also found in some SSEs on subduc-  
98 tion zones, e.g., the deep Manawatu and Kaimanawa SSEs on the Hikurangi subduction  
99 zone (Wallace, 2020). Here, we aim to improve fault slip mapping in space and time to  
100 contribute to the advancement of the study of fault slip processes using, yet underutilised,  
101 satellite InSAR observations.

102 In this research, we developed a new method to interpret directly wrapped phase  
103 InSAR observations to estimate the spatio-temporal fault slip, in particular, in the con-  
104 text of a favourable tectonic setting, continental seismic swarms (e.g., small-amplitude  
105 surface deformation signals and/or phase discontinuities due to surface ruptures). In-  
106 SAR has been used to map surface displacements with high spatial resolution and sub-  
107 sequently model fault slip. But so far, it is more common to estimate static slip distri-  
108 butions than jointly invert for the time-series of slip evolution (Floyd et al., 2016; Ingleby  
109 et al., 2020). The problem of retrieving time series of source parameters from non-simultaneous  
110 and temporally overlapped multi-sensor observations is ill-posed; however, the oscilla-  
111 tions of the solution caused by the rank deficiency of this problem can be reduced by ap-  
112 plying regularisation or temporal filtering (Samsonov & D'Oreye, 2012). Grandin et al.  
113 (2010) introduced a temporal smoothing scheme as an additional constraint to retrieve  
114 the time series of magma volume changes. Additionally, González et al. (2013) used trun-  
115 cated singular value decomposition (TSVD) to reject model space basis vectors associ-  
116 ated with small singular values. Instead of regularising the volume variation itself, they  
117 minimised the volume change rate, to avoid large discontinuities. Here, we improve pre-  
118 vious methods by a) regularising the fault slip distribution using a prescribed param-  
119 eterisation derived from a laboratory-based crack model, and b) introducing a statisti-  
120 cally optimal truncation criterion that allows to automatically separate signal and noise  
121 in the spatio-temporal fault slip distributions. We demonstrated the validity of this ap-

122 proach using synthetic experiments and comparing it against a compilation of published  
123 slip distribution models. Finally, we applied the new proposed methodology to the 2011  
124 Hawthorne seismic swarm (Nevada, USA). The 2011 Hawthorne seismic swarm is located  
125 at the central Walker Lane, which accommodates the Pacific-North American transform  
126 plate motion by oblique-normal faults and block rotations (Thatcher et al., 1999; Wes-  
127 nousky, 2005). The 2011 Hawthorne swarm consists of 10 M4+ events, and the largest  
128 earthquake among them is an M4.6 event (Zha et al., 2019; Smith et al., 2011); a recent  
129 study using satellite images reveals clear surface deformation signals before the M4.6 event,  
130 and the geodetic moment is much higher than the seismic moment, indicating that aseis-  
131 mic slip dominates the fault behaviour (Jiang & González, 2021). By applying our pro-  
132 posed methodology, we retrieved the fault-slip spatio-temporal evolution, and explored  
133 the interactions between the fault slip and the seismicity.

## 134 **2 Time-Dependent Fault Slip Inferred Using Geodetic Fault Slip Mod-** 135 **els**

### 136 **2.1 Static Fault Slip Models**

137 Slip inversions with kinematic models are ill-posed problems in which the solution  
138 is nonunique and unstable, and unphysical slip distributions can be estimated by least-  
139 squares algorithms, i.e., extremely rough oscillatory slip distributions. Harris and Segall  
140 (1987) introduced Laplacian smoothing as the regularisation scheme. This minimises the  
141 second derivative of slip and can prevent cases with large stress drops. Du et al. (1992)  
142 plotted a trade-off curve for misfit as a function of slip roughness, and manually picked  
143 a smoothing factor within the inflection point of the curve to find an optimal balance  
144 between data fit and model roughness. Matthews and Segall (1993) determined the op-  
145 timal smoothing factor in the trade-off curve objectively by implementing the cross-validation  
146 method. Much later, Fukahata and Wright (2008) and Fukuda and Johnson (2008) in-  
147 troduced the Bayesian approach, ABIC (Akaike’s Bayesian Information Criterion), to  
148 solve the slip distribution. While Fukahata and Wright (2008) emphasised the signifi-  
149 cance of fault geometry as a nonlinear constraint, Fukuda and Johnson (2008) overcame  
150 the deficiencies of ABIC with positivity constraints, and then applied the adapted ABIC  
151 to simultaneously estimate the slip distribution and smoothing parameter objectively in  
152 a Bayesian framework. Fukuda and Johnson (2010) then devised a mixed linear-non-linear  
153 Bayesian inverse formulation and extended their work for the joint slip and geometry in-

154 version. In response, Minson et al. (2013) argued that the non-physical regularisation  
155 scheme (i.e., Laplacian smoothing) is unnecessary, and developed a fully Bayesian ap-  
156 proach to sample all possible families of models compatible with the observations, via  
157 a parallel computing framework. Ragon et al. (2018) further extended the work of Minson  
158 et al. (2013) and accounted for the uncertainty in fault geometry. Instead of Laplacian  
159 regularisation, Amey et al. (2018) developed an inversion package *slipBERI*, and incor-  
160 porated self-similarity, characterising the seismic slip distribution in real earthquakes,  
161 as a prior assumption within the Bayesian inversion of earthquake slip.

162 All the previous methods are based on kinematic models that do not take into ac-  
163 count the relationship between stress and slip in the fault. Alternatively, dynamic source  
164 models satisfy physical constraints on the propagation of shear fractures on Earth, but  
165 few dynamic source models are considered to constrain the slip inversions. As an alter-  
166 native, Di Carli et al. (2010) proposed using elliptical patches to describe the slip dis-  
167 tribution in the kinematic and dynamic inversion of near-field strong motion data at low  
168 frequencies. Soon afterwards, Sun et al. (2011) put forward a *mechanical* slip inversion,  
169 imposing a uniform stress drop on the fault plane. The resulting slip distribution is in-  
170 herently smooth, so the smoothing norm and the smoothing factor are unnecessary. Tridon  
171 et al. (2016) assumed a circular stress patch in volcano research, inverting the displace-  
172 ment for shear and normal stresses simultaneously, along with the fault geometry.

173 In this study, we apply a new methodology named Geodetic fault-slip Inversion us-  
174 ing a physics-based Crack Model (GICMo) (Jiang et al., 2022). In this method, we take  
175 advantage of a one-dimensional analytical crack model proposed by Ke et al. (2020). The  
176 model was theoretically and experimentally validated in self-contained ruptures within  
177 a 3-meter-long saw-cut granite fault. This new crack model features non-singular (finite)  
178 peak stresses at the rupture tip. In Jiang et al. (2022), we expanded the one-dimensional  
179 model into two dimensions to produce elliptical fault slip shapes/patches. We assume  
180 that one of the focal points of the ellipse is the crack centre (with the maximum slip)  
181 and the elliptical perimeter to be the crack tip. Therefore, the slip distribution on the  
182 fault plane is controlled by a very compact and reduced set of parameters. The geodetic-  
183 inverted fault slip infers that it is possible that the crack centre can be located at the  
184 rupture centre, e.g., the 2009 L'Aquila earthquake (Walters et al., 2009). To adapt to  
185 this possibility, we relax the constraint that the maximum slip should coincide with the  
186 crack centre location, and allow it to move along the x axis inside the ellipse. Hence, our

187 crack model contains only eight parameters as demonstrated by Equation 1 and Figure 1.

$$s = \mathbf{f}(x_0, y_0, a, e, \alpha, \lambda, d_{max}, \theta) \quad (1)$$

188 where  $s$  is the slip distribution;  $x_0, y_0$  are the locations of the crack centre ;  $a$  and  $e$  are  
 189 the semi-major axis and eccentricity of the ellipse;  $\alpha$  is the ratio controlling the location  
 190 of the crack centre along x axis: the crack centre is located at the ellipse centre , left/right  
 191 vertices when  $\alpha = 0, -1/1$ ;  $\lambda$  is the ratio controlling the displacement transition from  
 192 the centre to the edge of the elliptical crack;  $d_{max}$  is the maximum slip;  $\theta$  is the rake an-  
 193 gle.

194 In the GICMo method, once the crack model parameters are provided, the slips  
 195 for all fault patches are then determined based on the two-dimensional crack model dis-  
 196 cussed above. Then, the fault slip distribution is forward modelled to estimate surface  
 197 displacement. Following Jiang and González (2020), a misfit function is constructed based  
 198 on the wrapped phase residuals and the weighting matrix. The misfit function is then  
 199 regarded as the likelihood function fed into the Bayesian process to retrieve the poste-  
 200 rior distribution of crack model parameters. In the Bayesian process, the Markov chain  
 201 Monte Carlo algorithm is adopted as the probability sampling approach based on the  
 202 Metropolis-Hasting rule.

203 Here we design a synthetic static slip to compare the performance of our method,  
 204 GICMo, and a state-of-the-art method, slipBERI (Amey et al., 2018). The geodetic in-  
 205 version package, slipBERI, solves for fault slip with GNSS and unwrapped InSAR phases  
 206 in a Bayesian approach using von Karman regularisation, and simultaneously solves for  
 207 a hyperparameter that controls the degree of regularisation. A normal fault with pure  
 208 down-dip slip is simulated as the synthetic fault model. To imitate the slipping patterns  
 209 observed in the published finite-source rupture models SRCMOD (Mai & Thingbaijam,  
 210 2014) (e.g., Bennett et al. (1995), Ichinose et al. (2003), and Elliott et al. (2010)), the  
 211 inner region is a square area with a larger displacement, and the outer region is an an-  
 212 nulus area with a smaller displacement (Figure 2). Due to the difference in the inges-  
 213 tion data, the synthetic phases are unwrapped phases for slipBERI and wrapped phases  
 214 for GICMo. The displacement phase is forward calculated based on the synthetic fault  
 215 slip distribution and the dislocation model. To increase its resemblance to reality, decor-  
 216 relation and atmosphere noises are simulated and added, whose amplitudes are 10% of  
 217  $2\pi$  for wrapped phase cases or the peak amplitude of the deformation phase for unwrapped

218 phase cases, which is based on the signal-to-noise ratio from a real interferogram in Sec-  
 219 tion 4 (RS2-20110322-20110415). The simulated noise-plus-deformation interferogram  
 220 is resampled with a quadtree algorithm within the downsampled unwrapped and wrapped  
 221 phases (Bagnardi & Hooper, 2018; Jiang & González, 2020). In addition, the covariance  
 222 matrix is estimated based on the phase in the far-field. Finally, the downsampled phases  
 223 and covariance matrix are fed into slipBERI and GICMo to retrieve the slip distribu-  
 224 tions. Figures 2b-2d show the modelled slip distribution inverted by GICMo and slip-  
 225 BERI, and Figure S1 shows the modelled phase and phase residuals. The conclusions  
 226 are listed below.

- 227 (1) Both GICMo and slipBERI provide the first-order accuracy of the slip distri-  
 228 bution, including the locations of the crack centre and the magnitude of the slip peak.
- 229 (2) We interpolate the slip distribution onto a  $0.5 \text{ km} \times 0.5 \text{ km}$  patch mesh, and  
 230 calculate the root-mean-square error (RMSE) of the slip distribution compared with the  
 231 synthetic slip distribution. We find that the RMSEs are 1.5 cm for the one-ellipse model,  
 232 2 cm for the von Karman smoothing model, and 3 cm for the Laplacian smoothing model,  
 233 which are approximately similar. However, the great advantage is that the parameters  
 234 to be solved in GICMo are independent of the fault mesh discretization, and the num-  
 235 ber of parameters is 30 times less in this case than 201 in slipBERI for this case.

## 236 **2.2 Bayesian Inversion of Fault Slip Time-Series Using a Physics-based** 237 **Crack Model (Time-GICMo)**

238 The temporal evolution of fault slip is critical to understanding the driving mech-  
 239 anism of slow slip. It is difficult to find one slow slip event where one interferogram can  
 240 coincidentally capture the beginning and the ending of the activity. Instead, a common  
 241 scenario is that the slip increment is captured by interferograms. In this section, we de-  
 242 velop a new method of retrieving the slip increments and demonstrate the time-series  
 243 slip estimation with synthetic experiments. Assuming two elliptical ruptures at the be-  
 244 ginning and the ending, slip increment  $\Delta s = s^2 - s^1$ , where  $s^2$  and  $s^1$  are the slip dis-  
 245 tributions at the end and the beginning of the interferogram.

246 We consider a system of  $N$  increments of fault slip ( $\Delta s^n \in [\Delta s^1, \dots, \Delta s^N]$ ) between  
 247 dates  $t_i^n$  and  $t_j^n$ ) based on the non-linear inversion estimation from the corresponding wrapped  
 248 interferogram, and the raw images of interferograms are acquired at  $M$  unique dates ( $t \in$   
 249  $[t_1, \dots, t_M]$ ). The aim is to solve for the temporal evolution of fault slips ( $s \in [s_1, \dots, s_M]$ )

250 for each date. We assume that the slip rate between adjacent dates ( $v_m \in [v_1, \dots, v_{M-1}]$ )  
 251 is constant, so the slip increment  $\Delta s^n$  can be expressed by the sum of fault slip incre-  
 252 ment between adjacent dates,  $\Delta s^n = \sum_{m=i}^{j-1} v_m (t_{m+1}^n - t_m^n)$ . The linear expression for  
 253  $N$  increments of fault slip is shown in Equation 2, as illustrated by González et al. (2013):

$$\begin{aligned} \mathbf{P} &= \mathbf{B}\mathbf{Q} \\ \mathbf{P} &= [\Delta s^1 \quad \dots \quad \Delta s^n \quad \dots \quad \Delta s^N]^T \\ \mathbf{Q} &= [v_1 \quad \dots \quad v_m \quad \dots \quad v_{M-1}]^T \\ \mathbf{B}(n, m) &= \begin{cases} t_{m+1}^n - t_m^n, & \text{if } i \leq m \leq j - 1. \\ 0, & \text{otherwise.} \end{cases} \end{aligned} \quad (2)$$

254 where  $\mathbf{P}$  is the observation vector,  $\mathbf{Q}$  is the unknown vector, and  $\mathbf{B}$  is the designed ma-  
 255 trix. Considering there are  $N$  increments of fault slip, the matrix dimension is  $(N \times 1)$   
 256 for  $\mathbf{P}$ ,  $(N \times (M - 1))$  for  $\mathbf{B}$ , and  $((M - 1) \times 1)$  for  $\mathbf{Q}$ . Then, we decompose matrix  $\mathbf{B}$   
 257 by using the SVD methods,

$$\mathbf{B} = \mathbf{U}\mathbf{S}\mathbf{V}^T \quad (3)$$

258 where  $\mathbf{U}$  is an orthogonal matrix with columns that are the basis vectors of the data space  
 259  $(N \times N)$ ,  $\mathbf{V}$  is an orthogonal matrix with columns that are the basis vectors spanning  
 260 the singular values of the model  $((M - 1) \times (M - 1))$ , and  $\mathbf{S}$  is a diagonal matrix of  
 261 the singular values  $((N \times (M - 1)) \times 1)$ . A solution for this problem can be obtained  
 262 as follows,

$$\mathbf{Q} = \mathbf{V}\mathbf{S}^{-1}\mathbf{U}^T\mathbf{P} \quad (4)$$

263 If  $\text{rank}(\mathbf{B}) < m$ , the solution obtained using the SVD technique may contain numerical  
 264 instabilities when there are small singular values. In this case, a more stable solution can  
 265 be achieved using the TSVD method (Aster et al., 2019), which rejects model space ba-  
 266 sis vectors associated with small singular values, up to a certain threshold. As an im-  
 267 provement upon González et al. (2013), we apply an optimal hard threshold for singu-  
 268 lar values truncation proposed by Gavish and Donoho (2014). Gavish and Donoho (2014)  
 269 proposed that the optimal hard threshold for singular value is  $4/\sqrt{3}$  of the median sin-  
 270 gular value. This criterion is empirically proven to be the best hard thresholding, inde-  
 271 pendent of model size, noise level, or true rank of the low-rank model. This improvement

272 allows us to define the degree of regularisation based on an objective criterion, which gener-  
 273 erates a parsimonious low-rank model solution in the presence of noisy data. Note that  
 274 in order to retrieve a realistic solution, a non-negative constraint is added in solving for  
 275 slip rate vector  $Q$  implemented by using MATLAB function *lsqnonneg* ([https://uk.mathworks](https://uk.mathworks.com/help/optim/ug/lsqnonneg.html)  
 276 [.com/help/optim/ug/lsqnonneg.html](https://uk.mathworks.com/help/optim/ug/lsqnonneg.html)). It is physically appropriate because slip along  
 277 faults rarely re-rupture backwards (Hicks et al., 2020).

### 278 **3 Time-dependent Fault Slip Inversion Experiments**

279 In this section, we describe two experiments to investigate if this method can re-  
 280 trieve pulse- and crack-like rupture propagation patterns in space and time. We tested  
 281 the performance of the inversion method to recover fault slip evolution from each of the  
 282 two-ellipse models.

283 The first synthetic case aims to explore the inversion with overlapping ruptures (Fig-  
 284 ure 3). Several recent studies have suggested spatial overlap between coseismic slip and  
 285 afterslip (Barnhart et al., 2016; Bedford et al., 2013; Bürgmann et al., 2002; Johnson et  
 286 al., 2012; Pritchard & Simons, 2006; Salman et al., 2017; Tsang et al., 2016). A series  
 287 of overlapping elliptical cracks are simulated in Figure 3a, and a forward inversion is per-  
 288 formed to calculate the surface displacement due to the slip increment between adjacent  
 289 cracks. We aimed to compare the results based on various geodetic inversion algorithms:  
 290 (1) the one-ellipse model, as described in Section 2.1, (2) a von Karman regularisation  
 291 algorithm (Amey et al., 2018), (3) the two-ellipse model with different crack centres.  
 292 Inversion results are shown in Figures 3b-3d, and the modelled phase and residuals are  
 293 shown in Figures S2-S3. The main conclusions are as follows.

294 (1) The RMSEs of the fault slip residual is the lowest in results based on the two-  
 295 ellipse model with different centres. The triangle patch size in the crack model is  $\sim 0.84$  km,  
 296 and the rectangle patch size in slipBERI is 1.5 km. In this way, we interpolated the mod-  
 297 elled slip distributions to grid points with 1.17 km spacing, and then calculated the RMSE  
 298 of the fault slip residual. In each case, the RMSE of slip residuals based on the two-ellipse  
 299 model with different centres (Figure 3d) are the smallest, and the average RMSE for the  
 300 one-ellipse model, the von Karman smoothing model and the two-ellipse model are 0.9 cm,  
 301 1.6 cm, and 0.6 cm.

302 (2) The two-ellipse model is superior to the one-ellipse model in the F-test for the  
 303 residual of the interferometric phase. The two-ellipse model has more free parameters,

304 leading to an inherent improvement in the data fit. To objectively compare the model  
 305 performances, we use the F-ratio statistic to test the significance of the decrease of resid-  
 306 uals between models (Stein & Gordon, 1984). The statistical test checks if the empir-  
 307 ical F-ratio ( $F_{emp}$ ) is larger than the theoretical ( $F_{theory}$ ). In this case, the comparison  
 308 of the one-ellipse model and two-ellipse model leads to  $F_{emp} = 72.8 \gg F_{theory} = 2.6$ .

309 The second synthetic case aims to explore the inversion with the containing rup-  
 310 tures (Figure 4). A growing rupture has been widely observed and studied in fluid in-  
 311 jection experiments (Guglielmi et al., 2015; Bhattacharya & Viesca, 2019; Cappa et al.,  
 312 2019). The rupture centre is located at the injection point, and the radius of the slip-  
 313 ping zone grows at a rate up to  $10^{-6}$  m/s. A set containing elliptical ruptures is sim-  
 314 ulated in Figure 4a, and a forward inversion facilitates the surface displacement calcu-  
 315 lation. We aimed to retrieve the slip increments from the observed interferometric phase  
 316 with various methods described above (one-ellipse model, von Karman smoothing model,  
 317 and two-ellipse model). On noticing that the slip distribution is not well resolved by the  
 318 two-ellipse model with different centre  $s$ , we added another constraint to the two-ellipse  
 319 model so that both cracks share the same centre  $s$ . The inversion results are shown in Fig-  
 320 ures 4b-4e, and the modelled phase and residuals are shown in Figures S4-S5. The main  
 321 conclusions are as follows.

322 (1) The average RMSE of slip residuals based on various inversion models (one-  
 323 ellipse model, von Karman smoothing model, two-ellipse model with different centre  $s$ ,  
 324 and one centre  $s$ ) are 1.3 cm, 1.3 cm, 1.0 cm, and 0.8 cm. The one-ellipse model failed  
 325 because the slip increment in containing ruptures no longer could be described by one  
 326 complete crack. Indeed, slipBERI showed better performance because it inferred the re-  
 327 gion with the slip peak. The two-ellipse model with different centres is even better but  
 328 was not well resolved, e.g., the slip increment from  $t_1$  to  $t_2$  (second image in Figure 4c).  
 329 Therefore, the two-ellipse model with the *same* centre is the most appropriate for recon-  
 330 structing the cracks' locations, sizes, and maximum slips.

331 (2) In the F-test of the interferometric phase residuals, the two-ellipse model with  
 332 the same centre is superior to the two-ellipse model with different centre  $s$ , and the one-  
 333 ellipse model is the least useful.

## 4 Application case: the 2011 Hawthorne Seismic Swarm (Nevada, USA)

### 4.1 Regional Tectonics and Seismicity

We apply our algorithm to the 2011 Hawthorne seismic swarm, which occurred on the central Walker Lane (Figure 5). The Walker Lane is a 500 km-long and 100 km-wide deformation region consisting of N-NW right-lateral shear and extension (Wesnousky, 2005). It is located between the northwest translating Sierra Nevada microplate and the westward extending Basin and Range Province. The Walker Lane accommodates 20%  $\sim$  25% of the current relative motion (50 mm/year) between the Pacific and North American plates (Argus & Gordon, 1991; Faults & Henry, 2008). The central Walker Lane accommodates the deformation budget of  $\sim$ 8 mm/year between the Basin and Range province and the central Sierra Nevada (Bormann et al., 2016). The distributed dextral shear in central Walker Lane is accommodated by oblique-normal faults, block rotations, and partitioning of oblique deformation between sub-parallel normal and strike-slip faults. The total long-term strain rate is 51 nanostrain/year extension directed N77°W and 38 nanostrain/year contraction directed N13°E (Kreemer et al., 2014), much higher than the central Basin and Range (Kreemer et al., 2009).

Being a geologically young and developing fault system, the Walker Lane shows high levels of seismicity over the instrument period, including  $>10$  M6+ earthquakes in the last century. Since 2000, the Walker Lane was struck by a few seismic sequences with some accompanied by aseismic slip evidence. For example, for the 2008 Mogul earthquake sequence, geodetic observation and modelling indicated significant aseismic slip (Bell et al., 2012), and the migration speed of the largest foreshock cluster is consistent with aseismic slip (Ruhl et al., 2016); for the 2014 Virginia City Swarm, migration rate of small earthquakes was consistent with rates observed elsewhere associated with pore fluid diffusion and aseismic creep (Hatch et al., 2020). However, there was no clear indication of aseismic slip during the 2016 Nine Mile Ranch sequence (Hatch-Ibarra et al., 2022), the 2017 Truckee sequence (Hatch et al., 2018) or the 2020 Monte Cristo Range sequence (Ruhl et al., 2021).

The 2011 Hawthorne seismic swarm lasted from March to September and consisted of 10 M4+ earthquakes according to the U.S. Geological Survey (USGS) hypocentre catalogue (<https://earthquake.usgs.gov/earthquakes/search/>). This sequence occurred in the footwall block of the Wassuk Range segment at the central Walker Lane (Faults

366 & Henry, 2008), and this segment experiences a significant extension of  $1.5\pm 0.3$  mm/year  
367 (Hammond & Thatcher, 2007). Early moment tensor solutions show the shallow depths  
368 in this sequence (Smith et al., 2011), and further hypocentre relocation together with  
369 the focal mechanisms of the M4+ events consistently reveal a W-NW-dipping normal  
370 fault zone with centroid depths between 2 km and 4 km (Zha et al., 2019). The 2011 Hawthorne  
371 sequence is close to the Aurora-Bodie volcano (Lange & Carmichael, 1996), but no vol-  
372 canic signature was observed in near-source seismograms, which infers this sequence is  
373 not likely related to the magmatic activity (Smith et al., 2011; Zha et al., 2019). In this  
374 research, we were able to identify three stages with respect to the timing of the most en-  
375 ergetic event (M4.6) occurred: an initial stage (pre-M4.6 stage) from 15 March to 17 April,  
376 a shorter period around the most energetic stage (co-M4.6 stage), and the post-energetic  
377 stage (post-M4.6 stage) lasting until 17 September.

## 378 4.2 Multi-satellite Geodetic Datasets

379 We processed ENVISAT and RADARSAT-2 data and generated 8 SAR interfer-  
380 ograms to quantify surface displacements (Figure 6). SAR images were acquired between  
381 February and September 2011 from two tracks: one ascending track from the Canadian  
382 Space Agency RADARSAT-2 satellite, look angle of  $35^\circ$  and heading angle of  $350^\circ$ ; and  
383 another descending track from the European Space Agency (ESA) ENVISAT satellite,  
384 track 343, look angle of  $35^\circ$  and heading angle of  $-166^\circ$ . Interferograms were processed  
385 in two-pass differential mode, using a 30 m resolution digital elevation model (DEM) de-  
386 rived from the Shuttle Radar Topography Mission. ENVISAT-ASAR data were processed  
387 using Doris software (Kampes et al., 2003) and ISCE software, RADARSAT-2 data us-  
388 ing GAMMA software (Werner, 2000). Overall, we obtained 8 short baseline differen-  
389 tial interferograms. The computed interferograms have temporal separations ranging from  
390 24 to 120 days. Considering the dominant extensional mechanism and N-S fault strik-  
391 ing in this region, the preferred movement direction of the ground displacement is E-W.  
392 Consequently, the satellite flight direction favours surface displacement observations in  
393 this normal faulting system.

394 Interestingly, 2 ascending RADARSAT-2 interferograms during the pre-M4.6 stage  
395 indicated clear surface displacement signals (Figure 6d and 6a),  $\sim 4$  cm away from satel-  
396 lite line-of-sight motion. In interferograms covering the co-M4.6 stage, it is notable that  
397 surface displacement signals were larger in magnitude and located further north with re-

398 spect to the pre-M4.6 stage (Figures 6b, 6c, 6e and 6f). During the early post-M4.6 stage,  
 399 surface displacements were detected along a very narrow spatial band with clear phase  
 400 discontinuities, suggesting surface ruptures (Figure 6g). For one interferogram covering  
 401 the late post-M4.6 stage (Figure 6h), the phase was dominated by atmospheric noise and  
 402 no clear deformation signal was detected. Analysis of interferograms suggests that fault  
 403 slip may have occurred along a fault system with a two-plane geometry, which is con-  
 404 sistent with the finding from early moment tensor solutions (Smith et al., 2011).

405 Note that the 2 ascending RADARSAT-2 interferograms provide a unique oppor-  
 406 tunity to look into the preseismic slip, which is not available in other reported cases due  
 407 to the data limitation. For example, for the 2008 Mogul earthquake swarm, Bell et al.  
 408 (2012) measured the surface deformation covering the whole earthquake swarm using In-  
 409 SAR and they found that the modelled cumulative geodetic moment is  $\sim 2$  times the cu-  
 410 mulative seismic moment, indicating a significant portion of aseismic slip. However, they  
 411 cannot separate the preseismic deformation signal because there is no available interfer-  
 412 ogram covering the preseismic stage only. In addition, the GPS observations covering  
 413 the 2008 Mogul earthquake swarm cannot constrain the preseismic slip well due to the  
 414 low signal to noise ratio in GPS solutions (Ruhl et al., 2016).

### 415 **4.3 Spatio-temporal Slip Evolution**

416 To develop the kinematic fault model, we first constructed the fault geometry de-  
 417 rived from a non-linear fault inversion of InSAR wrapped phase observations, solving for  
 418 uniform distribution on rectangular faults (Jiang & González, 2020). A geodetic inver-  
 419 sion directly using the interferometric wrapped phase avoids any potential phase unwrap-  
 420 ping error (Figure S6). The data variance-covariances describing the noise level are cal-  
 421 culated based on the covariograms (Figure S7) and are used to weight the wrapped phase  
 422 residuals in the likelihood function as illustrated by Jiang and González (2020). Mod-  
 423 elling of a selection of interferograms covering the successive phases confirmed that ground  
 424 motion could be caused by fault geometry with two distinct planes. During the pre-M4.6  
 425 stage, the observed ground motion in the RADARSAT-2 interferogram (2011/03/22-2011/04/15,  
 426 Figure 6d, and fault-normal profile in Figure 7d) would be consistent with slip along a  
 427 N-S striking normal fault to the south (green rectangular fault in Figure 7a). After mod-  
 428 elling the interferogram covering the co- and post-M4.6 stages (2011/04/15-2011/06/26,  
 429 Figure 6f, and fault-normal profile in Figure 7c), Figure 6f shows a different fault seg-

430 ment on a NE-SW trending normal fault to the north (yellow rectangular fault in Fig-  
 431 ure 7a). Only one single fault is applied in the modelling above, and the phase caused  
 432 by the northern subfault is modelled well due to its dominance during the co- and post-  
 433 M4.6 stages. The residual is relatively larger in the south because of the ignorance of  
 434 the southern subfault, as shown by the residual phases in Figure S8. Based on modelled  
 435 fault geometry in Figure 7a, together with ground motion discontinuities digitised from  
 436 the interferograms, we constructed a smooth fault plane with uniformly discretized tri-  
 437 angular meshes in Figure 7d. These were generated by FaultResampler (Barnhart & Lohman,  
 438 2010) and mesh2d (Engwirda, 2014), with a near-uniform side length of around 125 m.  
 439 Then, a fault slip distribution model with associated uncertainties was estimated. We  
 440 applied the fault slip inversion method based on a prescribed regularisation derived from  
 441 an experimentally validated physics-based crack model (Jiang et al., 2022). To further  
 442 investigate the temporal evolution of fault slips with a higher temporal resolution, we  
 443 invert the fault slip time series using all available interferograms with clear deformation  
 444 signals.

445 Figure 8 presents the temporal evolution of cumulative slip and slip rate during the  
 446 2011 Hawthorne seismic swarm, and Figure S9 shows the modelled phase and phase resid-  
 447 uals. The findings from the inversion results are listed as follows.

448 (1) There were three areas with different spatio-temporal slipping behaviours: a  
 449 narrow (5 km<sup>2</sup>) slip area on the southern fault with a high rate (with a lower bound: 1.5 cm/day,  
 450 or  $1.7 \times 10^{-7}$  m/s) occurring during the pre-M4.6 stage, a wider (15 km<sup>2</sup>) slip area with  
 451 lower average slip (10 cm) on the northern fault that ruptured during the co-M4.6 stage,  
 452 and a shallow slip area (depth=1 km) just above the second area during the post-M4.6  
 453 stage with a slower average slip rate (with a lower bound: 0.2 cm/day, or  $2.3 \times 10^{-8}$  m/s).

454 (2) Our results show the aseismic slip mainly occurred on the southern subfault dur-  
 455 ing the pre-M4.6 stage, while the most significant seismic slip hit the northern subfault  
 456 during the co- and post-M4.6 stages. The results are more consistent with a cascade model  
 457 of discrete slip patches, rather than a slow-slip model considered as a growing elliptical  
 458 crack.

459 (3) During the early pre-M4.6 stage (February 26-March 22), the cumulative geode-  
 460 tic moment is  $1.7 \times 10^{16}$  Nm (equivalent to an  $M_w$  4.7 event), 45 times as large as the cu-  
 461 mulative seismic moment ( $0.04 \times 10^{16}$  Nm). The cumulative geodetic/seismic moment ra-  
 462 tio reduces over time, but remains larger than 3 during the co- and post-M4.6 stages.

## 5 Discussion

### 5.1 On the Spatial Complexity of Fault Slip Distributions

Fault slip most likely has non-uniform spatial distribution due to spatial heterogeneities of rock strength and stress state on the fault, with well-known dependence on depth and the less understood along-strike variations. Seismic and geodetic inversions can reveal how fault slip is distributed on the discretized fault plane. However, to explore all possible models consistent with observations, the parameter space scales up rapidly to a large number of unknowns, increasing the problem's null-space, which means there are many vectors in the model space that are unconstrained by the data. Therefore, it is reasonable to consider our understanding of the complexity of slip distribution in natural earthquakes. The reasonable approach can allow for fault-slip heterogeneity while keeping the problem null-space as small as possible. Mai and Beroza (2002) compiled published finite-source rupture models and proposed the fractal pattern in slip distributions. It is true for large earthquakes, and multiple fault segments with several rupturing centres are revealed by geodetic and seismological observations, e.g., the 2008  $M_w$ 7.9 Wenchuan earthquake (Shen et al., 2009), and the 2016  $M_w$ 7.8 Kaikoura earthquake (Hamling et al., 2017). However, solving a huge number of parameters has a high computation cost. Computation complexities in their algorithms depend greatly on the number of discretized fault patches. For example, when studying a 40 km-long and 20 km-wide fault with slip-BERI, there are 200 patches if the patch size is 2 km and the parameter's dimension is 400. The latter would rapidly increase to 1600 if the patch size is 1 km. This is possibly the reason why the number of imported fault patches has upper bounds in practice, particularly if a Bayesian sampling strategy is employed. Though techniques like parallel computing have been introduced to improve computation efficiency, sampling such high-dimensional problems is still computationally challenging and does not solve the size of the null-space.

In this research effort, we favoured a method that dramatically reduces the number of free parameters to solve; the drawback is that it results in *compact* fault slip distributions. However, our inverted slip distribution patterns are supported by the observations. This is a reasonable approach because many inversion results support fault-slip distributions that are spatially compact, especially for small-magnitude earthquakes (Taymaz et al., 2007; Barnhart et al., 2014; Xu et al., 2016; Champenois et al., 2017; Ainscoe et

495 al., 2017). Many studies have successfully modelled the majority of surface displacement  
496 signals using only one single fault with uniform distribution (Biggs et al., 2006; Nissen  
497 et al., 2007; Walters et al., 2009). For slow slip events across the global subduction zones,  
498 distribution patterns usually follow an elliptical shape with one slipping centre (Wallace  
499 et al., 2012; Villegas-Lanza et al., 2016; Fukuda, 2018), and the fractal pattern is not re-  
500 quired.

501 Benefiting from the online database of finite fault rupture models, SRCMOD (Mai  
502 & Thingbaijam, 2014), we were able to quantitatively evaluate how well a single ellip-  
503 tical model fits the available slip distributions across various tectonic settings and mag-  
504 nitudes. We retrieved 300 slip distributions on a single fault from SRCMOD and intended  
505 to model the slip distributions with the one-ellipse model. Our experiments showed that  
506 for 85% of  $M_w \leq 7.5$  events, the RMSE of the slip residual is less than 20% of the peak  
507 slip (Figure S10). In addition, a simple circular crack is also the widely accepted assumed  
508 model in stress drop estimation based on seismic spectra (Madariaga, 1976; Kaneko &  
509 Shearer, 2014). Though only small degrees of freedom are allowed in the one-ellipse model,  
510 complexity could be added by incorporating multiple ruptures. As we showed in Section  
511 2.2, a half-moon pattern was retrieved by two containing or overlapping elliptical crack  
512 models. Similarly, it is possible to overlap multiple ruptures to simulate multiple peak  
513 slips or more complex patterns.

514 The compact slip distribution in this new elliptical model is also favourable to eval-  
515 uate the statistics of small earthquakes. Earthquake source parameters characterisation  
516 of small earthquakes is important for understanding the physics of source processes and  
517 might be useful for earthquake forecasting (Uchide et al., 2014). A wide-used source model  
518 to analyse the source parameters of small earthquakes is a circular crack rupture (Brune,  
519 1970; Madariaga, 1976) with stress singularity at the crack tip, and we hope our new el-  
520 liptical slip model, which avoids this stress singularity, can be an alternative source model  
521 in the future (Shearer et al., 2006). Furthermore, by taking advantage of the improved  
522 method for estimating slip rates during temporally overlapping InSAR timeframes, one  
523 can image the fault behaviour over a long period in a relatively high temporal resolu-  
524 tion. This new method is expected to be applied to investigate the temporal evolution  
525 of slow fault slip, e.g., transient slow slip (Khoshmanesh et al., 2015; Kyriakopoulos et  
526 al., 2013; Klein et al., 2018), afterslip (Thomas et al., 2014), and slow slip events in sub-  
527 duction zones (Bletery & Nocquet, 2020; Rousset et al., 2019; Ozawa et al., 2019).

## 5.2 Time-dependent Fault Kinematics during Continental Seismic Swarms and Other Slow Earthquakes

During the initial stage of the 2011 Hawthorne seismic swarm, a substantial amount of aseismic slip ruptured on the southern subfault without strong seismicity (e.g., the first two periods in Figure 8b), with peak slip rates of 1.1~5.4 cm/day, average slip rate 0.4~1.9 cm/day and migration velocity 0.05 km/day. Note that these values are lower bounds, as the time between two neighbouring epochs ( $\Delta s^n$ ) of SAR image acquisition time may be longer than the duration of slow slip events, preventing capture of short events with higher velocities. The limitation due to the temporal sampling of InSAR could be improved by combining all of the InSAR datasets, or incorporating other high-temporal resolution observations, e.g., GNSS or strainmeter observations. We anticipate that the current InSAR temporal sampling limitation will be reduced over the second half of this decade (2020s). Our approach will be well suited to fully utilise the multiconstellation of InSAR capable satellites (Sentinel-1, CosmoSky-Med, PAZ, TerraSAR-X, ALOS-2, ALOS-4, NISAR, etc.). The phenomena potentially driven by aseismic slip are widely explored, e.g., ETS, Rapid Tremor Reversals (RTRs), SSEs, fault creep, and fluid injection. To better compare this precursory aseismic slip with other identified phenomena in the slow slip family, we compile the slip rates and migration velocities found in the literature (list below and in Table S1).

(1) The peak slip rate. SSEs show a wide range of peak slip rates among subduction zones, e.g., 0.27 cm/day for the Cascadia subduction zone (Bletery & Nocquet, 2020), 0.3 cm/day for South Central Alaska Megathrust (Rousset et al., 2019), 0.6~2.8 cm/day for Japan trench (Hirose & Obara, 2010; Ozawa et al., 2019). During the early stage of the 2011 Peloponnese seismic swarm (Greece) (Kyriakopoulos et al., 2013), the fault behaviour was dominated by aseismic slip inferred from the geodetic and seismic moment, and the peak slip rate was 0.26 cm/day. The maximum slip rate in fault creep events is very low, e.g., 0.5 cm/year on the Hayward fault (Schmidt et al., 2005), 0.5 cm/year on the Haiyuan Fault (Jolivet et al., 2012; Song et al., 2019), 0.8 cm/year on the North Anatolia Fault (Hussain et al., 2016) and 3 cm/year on the San Andreas Fault (Johanson & Bürgmann, 2005; Khoshmanesh et al., 2015; Scott et al., 2020). However, in the fluid injection experiment the slow aseismic slip during the early stage was much higher,  $4 \times 10^{-3}$  mm/s (35 cm/day) (Guglielmi et al., 2015), potentially because the measurement

560 in the fluid injection is real-time, and the duration uncertainty is much lower than SSEs  
 561 observations.

562 (2) The average rate of slip increment. Research on the 2010-2014 seismic swarm  
 563 in southern Italy (Cheloni et al., 2017) is consistent with our findings. This research re-  
 564 vealed that the average slip rate started to increase two months before the largest shock  
 565 ( $M_w$ 5.1) and reached the highest value,  $\sim 0.1$  cm/day, a few days before the largest shock.  
 566 It then decreased to zero in the following months. This highest average slip rate was at  
 567 the same level with  $\sim 0.4$ - $1.9$  cm/day in our research. The aseismic slip rate inferred by  
 568 SSEs is lower,  $\sim 0.03$ - $0.14$  cm/day (Radiguet et al., 2011), and this value is much lower  
 569 inferred by RE,  $\sim 0.3$ - $3$  cm/year (Nadeau & McEvilly, 1999; Turner et al., 2013; Mes-  
 570 imeri & Karakostas, 2018).

571 (3) Migration velocity. These velocities of ETS and SSEs vary with subduction zones  
 572 (Yamashita et al., 2015), but the generally reported migration velocity along the strike  
 573 of the plate geometry is  $\sim 10$  km/day (Wech et al., 2009), while RTRs propagate ‘back-  
 574 wards’ 20 to 40 times faster than ETS advances (Houston et al., 2011). The large-scale  
 575 features of ETS propagation with RTRs are reproduced and supported by numerical ex-  
 576 periments (Luo & Liu, 2019; Liu et al., 2020). Similarly, migration velocity in TES varies  
 577 over a wide range, from 0.5 to 14 km/day (Passarelli et al., 2018; De Barros et al., 2020).

### 578 **5.3 Spatially variable mechanical response of the Hawthorne swarm faults**

579 As shown in Figure 8b, the southern segment is active during the pre-M4.6 stage,  
 580 and the fault behaviour is mostly dominated by aseismic slip, inferred from a very high  
 581 geodetic/seismic moment ratio, 45 (Figure 8c), while the general cumulative geodetic/seismic  
 582 moment ratio remains larger than three for the whole seismic swarm. This significant  
 583 portion of aseismic slip identified here has been reported to explain the discrepancy be-  
 584 tween the geodetic moment and the seismic moment in a handful of continental seismic  
 585 swarms (Lohman & McGuire, 2007; Wicks et al., 2011; Kyriakopoulos et al., 2013; Gua-  
 586 landi et al., 2017; Cheloni et al., 2017). In 2005, a tectonic swarm of over a thousand earth-  
 587 quakes occurred in the Salton Trough, California (USA) and Lohman and McGuire (2007)  
 588 revealed the geodetic moment of the modelled fault system was about seven times the  
 589 cumulative seismic moment of the swarm. Wicks et al. (2011) studied a swarm in south-  
 590 eastern Washington (USA) and also found the geodetic/seismic moment ratio was about

591 seven. During the 2011 Peloponnese Peninsula seismic swarm (Greece), Kyriakopoulos  
592 et al. (2013) revealed a big discrepancy in moment release, where the geodetic moment  
593 was  $\sim 5$  times the cumulative seismic moment for the interval July 3-October 1. For the  
594 2013-2014 Northern Apennines seismic swarm (Italy), the moment associated with aseis-  
595 mic deformation/the seismic moment ratio is between  $70\% \pm 29\%$  and  $200\% \pm 70\%$  (Gualandi  
596 et al., 2017). For the 2010-2014 Pollino seismic swarm (Italy), Cheloni et al. (2017) found  
597 that 70% of the moment was released aseismically. Above all, previous studies require  
598 aseismic slip to explain the discrepancy between the geodetic moment and seismic mo-  
599 ment for seismic swarms, with the estimated ratio of  $\sim 1.7-7$ . Furthermore, the compact  
600 fault slip identified during the pre-M4.6 stage is favoured by our improved methodology  
601 as demonstrated in Section 2. The previous finding of fractal distribution of fault slip  
602 is based on M5.9+ earthquakes (Mai & Beroza, 2002), while small-to-moderate-magnitude  
603 ruptures would have a more compact slip distribution with low complexity as observed  
604 in the rupture models SRCMOD (Mai & Thingbaijam, 2014). Therefore, we hope that  
605 our improved method can be used to improve the detection of similar small-to-moderate-  
606 magnitude aseismic transients in future seismic swarms.

607 The large disagreement between the geodetic moment and the seismic moment in-  
608 dicates that aseismic slip dominates the fault behaviour during the early stage of the 2011  
609 Hawthorne seismic swarm, and seismic slip cannot solely explain the observed surface  
610 deformation successfully. Thus, the nucleation of the M4.6 event does not follow the cas-  
611 cading model, which only depends on the stress transfer caused by neighbouring fore-  
612 shocks and aseismic slip is not involved. Here we test whether the nucleation of the M4.6  
613 event follows another earthquake nucleation hypothesis, the preslip model, where the stress  
614 transfer caused by aseismic slip is responsible for the largest shock's occurrence. We utilise  
615 the cumulative slip distribution from our inversion model and compute the Coulomb stress  
616 change on the fault geometry as shown in Figure 8. The cumulative fault slip caused a  
617 Coulomb stress increase over the seismic rupture region of the M4.6 event and the max-  
618 imum value is  $4.1 \text{ MPa} > 0.01 \text{ MPa}$ , which is enough to trigger an earthquake (King et  
619 al., 1994). In addition, we compute the Coulomb stress change caused by a seismic slip  
620 of foreshocks on the fault geometry, and we find that the maximum Coulomb stress in-  
621 crease over the seismic rupture region of the M4.6 event is  $1.5 \text{ MPa} > 0.01 \text{ MPa}$ , so the  
622 cascading model may also play a role in the nucleation process. Note that the stress change  
623 analysis based on foreshocks' locations can be affected by many factors, e.g., the preci-

624 sion of earthquake hypocentre, and the stress drop calculation method. For example, an  
625  $M_w$ 4.3 foreshock occurred two hours before the 1992  $M_w$ 6.1 Joshua Tree earthquake, and  
626 there are opposite conclusions on whether the mainshock is triggered by the foreshock,  
627 by using different spatial resolutions in the foreshock-location-based analysis performed  
628 by Dodge et al. (1996) and Mori (1996). Therefore, because the Coulomb stress increase  
629 cause by aseismic slip is larger than that caused by seismic slip,  $4.1 \text{ MPa} > 1.5 \text{ MPa}$ , we  
630 interpret that the largest M4.6 event could have been triggered by earthquake nucleation  
631 initiated by aseismic slip, but the nearby preceding foreshocks likely also contributed to  
632 the nucleation process.

633 The aseismic slip mainly occurred on the southern subfault during the pre-M4.6  
634 stage, while the most significant seismic slip hit the northern subfault during the co- and  
635 post-M4.6 stages. Here we discuss the possible underlying mechanisms of contrasting be-  
636 haviours on the two subfaults. One potential cause of the precursory aseismic slip on the  
637 southern segment is various dilatancy properties along the strike. Many authors have  
638 studied the shear-induced dilatancy, which could increase the effective normal stress and  
639 thus favour fault stability (Segall & Rice, 1995; Segall et al., 2010; Ciardo & Lecampion,  
640 2019). For example, to explain abundant microseismicity and aseismic transients in bar-  
641 rier zones on the Gofar transform fault, Liu et al. (2020) proposed a numerical model  
642 where strong dilatancy strengthening effectively stabilizes along-strike seismic rupture  
643 propagation and results in rupture barriers where aseismic transients arise. If this is also  
644 true for the 2011 Hawthorne seismic swarm, the shear-induced dilatancy would explain  
645 the aseismic transients on the southern fault and the seismic rupture on the northern  
646 subfault. What's more, the requirement of enhanced fluid-filled porosity for the dilatancy  
647 strengthening might be filled for the 2011 Hawthorne sequence. The 2011 Hawthorne  
648 sequence is close to the Aurora-Bodie volcano (Lange & Carmichael, 1996), and geother-  
649 mal fluids have been found in this area (Hinz et al., 2010), so it is possible that excess  
650 fluids can be persistently supplied and lead to large fluid-filled porosity and high pore  
651 pressure. Therefore, the dilatancy strengthening might be one of the underlying mechan-  
652 ics that govern the partitioning between aseismic and seismic slip during the 2011 Hawthorne  
653 earthquake swarm.

654 In addition, the fault geometrical complexity could favour the lateral variation of  
655 slip and aseismic slip. Firstly, Romanet et al. (2018) proposed that two overlapping faults  
656 can naturally result in a complex seismic cycle without introducing complex frictional

657 heterogeneities on the fault. They found that for two mildly rate-weakening faults with  
658 a small distance between the faults, a complex behaviour with a mixture of slow and rapid  
659 slip can be observed. This finding is consistent with the mixture of slow and fast slip close  
660 to the connecting region of two subfaults during the 2011 Hawthorne swarm (triangu-  
661 lar subfault in Figure 8). Secondly, Cattania and Segall (2021) highlights the effect of  
662 long-wavelength fault roughness on a range of fault behaviours, foreshocks, and precu-  
663 rsory slow slip, during the preparation stage of an energetic event. Their numerical sim-  
664 ulation suggested the preparation stage is characterised by feedback between creep and  
665 foreshocks: episodic seismic ruptures break neighbouring asperity groups and favour the  
666 creep acceleration, which loads other asperities leading to further foreshocks consecu-  
667 tively. The coexistence of foreshocks and precursory slow slip, as well as their migration  
668 toward the hypocentre of the energetic event in Cattania and Segall (2021), also matched  
669 our observation during the pre-4.6 stage (Figure 8). Therefore, we think fault geomet-  
670 rical complexity might contribute to the precursory slow slip during the 2011 Hawthorne  
671 earthquake swarm.

## 672 **6 Conclusion**

673 This study developed a new methodology for estimating time-dependent fault slip  
674 distributions, by incorporating a physics-based crack model as a regularisation term. We  
675 first introduce two propagation patterns of fault ruptures and then propose a method  
676 to solve the complex slip distribution with multiple physics-based crack models. Finally,  
677 the performance of the proposed methodology is analysed with simulated experiments  
678 and geodetic observations during a real seismic swarm case. The advantages of the pro-  
679 posed method are as follows.

680 (1) The estimated fault slip solutions describe a compact slip distribution, due to  
681 the use of a laboratory-derived crack model. This choice significantly reduces the num-  
682 ber of parameters to solve, independently of the subsequent level of fault discretization.  
683 Though the slip complexity is less than in the previous methods, the additional complex-  
684 ity in the slip pattern can be incorporated by incorporating multiple partially or totally  
685 overlapping elliptical cracks.

686 (2) The robustness of our method has been analysed by a) its capability to repro-  
687 duce synthetic simulated cases with various slip patterns, and by b) the ability of ellip-  
688 tical slip patterns to reproduce published slip distribution from the SRCMOD database.

689 (3) Our proposed method is applied to estimate a detailed time-dependent fault slip dis-  
690 tribution model for the 2011 Hawthorne seismic swarm (Nevada, USA). Our results in-  
691 dicate that the seismic swarm was caused by activity on a two subfault network with dif-  
692 ferent orientations. The results also show that aseismic slip on a southern subfault dom-  
693 inates the fault behaviour during a pre-M4.6 stage; after the aseismic pulse (during the  
694 most energetic stage), the largest event occurred on a northern subfault. Our results are  
695 consistent with an overlapping fault slip migration during the preM4.6 stage along the  
696 southern fault, followed by larger triggered coseismic ruptures of fault patches along the  
697 northern fault. Our model is consistent with small-scale spatially compact fault slip dis-  
698 tribution and allows us to estimate lower bounds for the peak and average value of fault  
699 slip rates. These lower-bound estimates are consistent with reported values for slow slip  
700 events and other continental swarms.

701 The new inversion method presented here is complementary to the existing method-  
702 ologies to estimate fault-slip distributions using geodetic data. We hope that this approach  
703 will be particularly useful with current and near-future multiconstellation InSAR satel-  
704 lite radar interferometry missions. In this near-future context, this tool could improve  
705 the identification of similar precursory (aseismic) slow slip during other long-lasting earth-  
706 quake sequences (swarms), and help understand the driving mechanisms of earthquakes.

### 707 **Acknowledgments**

708 This research was supported by the Natural Environmental Research Council (NERC)  
709 through the centre for the Observation and Modelling of Earthquakes, Volcanoes and  
710 Tectonics (UK) (GA/13/M/031) and the LiCS large grant (NE/K011006/1). This re-  
711 search was also supported by a Chinese Scholarship Council-University of Liverpool joint  
712 scholarship awarded to YJ (201706450071). PJG acknowledged the support of the Span-  
713 ish Ministerio de Ciencia e Innovación research project, grant agreement number PID2019-  
714 104571RA-I00 (COMPACT) and the Beca Leonardo a Investigadores y Creadores Cul-  
715 turales 2020 from the Fundación BBVA. RADARSAT-2 images were acquired under SOAR-  
716 E project 28209 from the Canadian Space Agency, and ENVISAT images from ESA CAT1  
717 project 6745. RADARSAT-2 and ENVISAT interferograms in the paper can be down-  
718 loaded from <https://doi.org/10.5281/zenodo.5043161>. The finite-fault source model  
719 SRCMOD is retrieved from <http://equake-rc.info/srcmod/>. The geodetic inversion  
720 software slipBERI is retrieved from <https://github.com/ruthamey/slipBERI> and WG-  
721 BIS package from <https://doi.org/10.5281/zenodo.3727158>. The CRUST 1.0 model

722 is retrieved from <https://igppweb.ucsd.edu/~gabi/crust1.html>. The manuscript was  
723 edited by Guido Jones, currently funded by the Cabildo de Tenerife, under the TFinnova  
724 Programme supported by MEDI and FDCAN funds. Thanks go to Mehdi Nikkhoo for  
725 providing the triangular dislocation functions for the displacement gradient tensor. The  
726 authors are also grateful to Tim Wright, Dan Faulkner, and Louisa Brotherson for in-  
727 sightful discussions of different aspects of this study, as well as to editor Rachel Aber-  
728 crombie, associate editor, Eric Lindsey, and another anonymous reviewer for their help-  
729 ful and constructive reviews, which greatly improved this manuscript.

## References

- 730
- 731 Ainscoe, E. A., Elliott, J. R., Copley, A., Craig, T. J., Li, T., Parsons, B. E., &  
 732 Walker, R. T. (2017). Blind Thrusting, Surface Folding, and the Devel-  
 733 opment of Geological Structure in the Mw 6.3 2015 Pishan (China) Earth-  
 734 quake. *Journal of Geophysical Research: Solid Earth*, *122*(11), 9359–9382. doi:  
 735 10.1002/2017JB014268
- 736 Amey, R. M. J., Hooper, A., & Walters, R. J. (2018). A Bayesian Method for Incor-  
 737 porating Self-Similarity into Earthquake Slip Inversions. *Journal of Geophysi-  
 738 cal Research: Solid Earth*, *123*(7), 6052–6071. doi: 10.1029/2017JB015316
- 739 Argus, D. F., & Gordon, R. G. (1991). Current Sierra Nevada-North America mo-  
 740 tion from very long baseline interferometry: Implications for the kinematics of  
 741 the western United States. *Geology*, *19*(11), 1085–1088.
- 742 Aster, R. C., Borchers, B., & Thurber, C. H. (2019). Chapter Three - Rank De-  
 743 ficiency and Ill-Conditioning. In R. C. Aster, B. Borchers, & C. H. Thurber  
 744 (Eds.), *Parameter Estimation and Inverse Problems* (Third Edition ed., p. 55-  
 745 91). Elsevier. doi: 10.1016/B978-0-12-804651-7.00008-0
- 746 Bagnardi, M., & Hooper, A. (2018). Inversion of Surface Deformation Data for  
 747 Rapid Estimates of Source Parameters and Uncertainties: A Bayesian Ap-  
 748 proach. *Geochemistry, Geophysics, Geosystems*, *19*(7), 2194–2211. doi:  
 749 10.1029/2018GC007585
- 750 Barnhart, W. D., Benz, H. M., Hayes, G. P., Rubinstein, J. L., & Bergman,  
 751 E. (2014). Seismological and geodetic constraints on the 2011 Mw5.3  
 752 Trinidad, Colorado earthquake and induced deformation in the Raton Basin.  
 753 *Journal of Geophysical Research: Solid Earth*, *119*(10), 7923–7933. doi:  
 754 10.1002/2014JB011227
- 755 Barnhart, W. D., & Lohman, R. B. (2010). Automated fault model discretization  
 756 for inversions for coseismic slip distributions. *Journal of Geophysical Research:  
 757 Solid Earth*, *115*(B10). doi: 10.1029/2010JB007545
- 758 Barnhart, W. D., Murray, J. R., Briggs, R. W., Gomez, F., Miles, C. P., Svarc, J.,  
 759 ... Stressler, B. J. (2016). Coseismic slip and early afterslip of the 2015 Il-  
 760 lapel, Chile, earthquake: Implications for frictional heterogeneity and coastal  
 761 uplift. *Journal of Geophysical Research: Solid Earth*, *121*(8), 6172–6191. doi:  
 762 10.1002/2016JB013124

- 763 Bedford, J., Moreno, M., Baez, J. C., Lange, D., Tilmann, F., Rosenau, M., ... Vi-  
 764 gny, C. (2013). A high-resolution, time-variable afterslip model for the 2010  
 765 Maule Mw=8.8, Chile megathrust earthquake. *Earth and Planetary Science*  
 766 *Letters*, *383*, 26–36. doi: 10.1016/j.epsl.2013.09.020
- 767 Bell, J. W., Amelung, F., & Henry, C. D. (2012). InSAR analysis of the 2008  
 768 Reno-Mogul earthquake swarm: Evidence for westward migration of Walker  
 769 Lane style dextral faulting. *Geophysical Research Letters*, *39*(18). doi:  
 770 10.1029/2012GL052795
- 771 Bennett, R. A., Reilinger, R. E., Rodi, W., Yingping Li, Toksoz, M. N., & Hudnut,  
 772 K. (1995). Coseismic fault slip associated with the 1992 Mw 6.1 Joshua Tree,  
 773 California, earthquake: Implications for the Joshua Tree-Landers earthquake  
 774 sequence. *Journal of Geophysical Research: Solid Earth*, *100*(B4), 6443–6461.  
 775 doi: 10.1029/94JB02944
- 776 Bhattacharya, P., & Viesca, R. C. (2019). Fluid-induced aseismic fault slip out-  
 777 paces pore-fluid migration. *Science*, *364*(6439), 464–468. doi: 10.1126/science  
 778 .aaw7354
- 779 Biggs, J., Bergman, E., Emmerson, B., Funning, G. J., Jackson, J., Parsons, B.,  
 780 & Wright, T. J. (2006). Fault identification for buried strike-slip earth-  
 781 quakes using InSAR: The 1994 and 2004 Al Hoceima, Morocco earth-  
 782 quakes. *Geophysical Journal International*, *166*(3), 1347–1362. doi:  
 783 10.1111/j.1365-246X.2006.03071.x
- 784 Bletery, Q., & Nocquet, J. M. (2020). Slip bursts during coalescence of slow slip  
 785 events in Cascadia. *Nature Communications*, *11*(1), 1–6. doi: 10.1038/s41467  
 786 -020-15494-4
- 787 Bormann, J. M., Hammond, W. C., Kreemer, C., & Blewitt, G. (2016). Accom-  
 788 modation of missing shear strain in the Central Walker Lane, western North  
 789 America: Constraints from dense GPS measurements. *Earth and Planetary*  
 790 *Science Letters*, *440*, 169–177. doi: 10.1016/j.epsl.2016.01.015
- 791 Brune, J. N. (1970). Tectonic stress and the spectra of seismic shear waves from  
 792 earthquakes. *Journal of Geophysical Research*, *75*(26), 4997–5009. doi: 10  
 793 .1029/JB075I026P04997
- 794 Bürgmann, R., Ergintav, S., Segall, P., Hearn, E., McClusky, S., Reilinger, R., ...  
 795 Zschau, J. (2002). Time-Dependent Distributed Afterslip on and Deep be-

- 796 low the İzmit Earthquake Rupture. *Bulletin of the Seismological Society of*  
797 *America*, 92, 126–137. doi: 10.1785/0120000833
- 798 Caballero, E., Chounet, A., Duputel, Z., Jara, J., Twardzik, C., & Jolivet, R.  
799 (2021). Seismic and Aseismic Fault Slip During the Initiation Phase of the  
800 2017 Mw=6.9 Valparaíso Earthquake. *Geophysical Research Letters*, 48(6),  
801 e2020GL091916. doi: 10.1029/2020GL091916
- 802 Cappa, F., Scuderi, M. M., Collettini, C., Guglielmi, Y., & Avouac, J. P. (2019).  
803 Stabilization of fault slip by fluid injection in the laboratory and in situ. *Sci-*  
804 *ence Advances*, 5(3), eaau4065. doi: 10.1126/sciadv.aau4065
- 805 Cattania, C., & Segall, P. (2021). Precursory slow slip and foreshocks on rough  
806 faults. *Journal of Geophysical Research: Solid Earth*, e2020JB020430. doi: 10  
807 .1029/2020JB020430
- 808 Champenois, J., Baize, S., Vallee, M., Jomard, H., Alvarado, A., Espin, P.,  
809 ... Audin, L. (2017). Evidences of Surface Rupture Associated with a  
810 Low-Magnitude (Mw 5.0) Shallow Earthquake in the Ecuadorian Andes.  
811 *Journal of Geophysical Research: Solid Earth*, 122(10), 8446–8458. doi:  
812 10.1002/2017JB013928
- 813 Cheloni, D., D’Agostino, N., Selvaggi, G., Avallone, A., Fornaro, G., Giuliani,  
814 R., ... Tizzani, P. (2017). Aseismic transient during the 2010-2014  
815 seismic swarm: Evidence for longer recurrence of  $M \geq 6.5$  earthquakes in  
816 the Pollino gap (Southern Italy)? *Scientific Reports*, 7(1), 1–10. doi:  
817 10.1038/s41598-017-00649-z
- 818 Ciardo, F., & Lecampion, B. (2019). Effect of Dilatancy on the Transition from  
819 Aseismic to Seismic Slip Due to Fluid Injection in a Fault. *Journal of Geophys-*  
820 *ical Research: Solid Earth*, 124(4), 3724–3743. doi: 10.1029/2018JB016636
- 821 De Barros, L., Cappa, F., Deschamps, A., & Dublanchet, P. (2020). Imbricated  
822 Aseismic Slip and Fluid Diffusion Drive a Seismic Swarm in the Corinth Gulf,  
823 Greece. *Geophysical Research Letters*, 47(9). doi: 10.1029/2020GL087142
- 824 Delorey, A. A., van der Elst, N. J., & Johnson, P. A. (2017). Tidal triggering of  
825 earthquakes suggests poroelastic behavior on the San Andreas Fault. *Earth*  
826 *and Planetary Science Letters*, 460, 164–170. doi: 10.1016/j.epsl.2016.12.014
- 827 Di Carli, S., François-Holden, C., Peyrat, S., & Madariaga, R. (2010). Dynamic  
828 inversion of the 2000 Tottori earthquake based on elliptical subfault ap-

- 829       proximations.     *Journal of Geophysical Research*, *115*(B12), B12328.     doi:  
830       10.1029/2009JB006358
- 831     Dodge, D. A., Beroza, G. C., & Ellsworth, W. L.     (1996).     Detailed observations of  
832       California foreshock sequences: Implications for the earthquake initiation pro-  
833       cess.     *Journal of Geophysical Research: Solid Earth*, *101*(B10), 22371–22392.  
834       doi: 10.1029/96JB02269
- 835     Du, Y., Aydin, A., & Segall, P.     (1992).     Comparison of various inversion techniques  
836       as applied to the determination of a geophysical deformation model for the  
837       1983 Borah Peak earthquake.     *Bulletin of the Seismological Society of America*,  
838       *82*(4), 1840–1866.
- 839     Elliott, J. R., Walters, R. J., England, P. C., Jackson, J. A., Li, Z., & Parsons, B.  
840       (2010).     Extension on the Tibetan plateau: recent normal faulting measured by  
841       InSAR and body wave seismology.     *Geophysical Journal International*, *183*(2),  
842       503–535. doi: 10.1111/j.1365-246X.2010.04754.x
- 843     Engwirda, D.     (2014).     *Locally optimal Delaunay-refinement and optimisation-based*  
844       *mesh generation* (Doctoral dissertation, University of Sydney). Retrieved from  
845       <http://hdl.handle.net/2123/13148>
- 846     Faulds, J., & Henry, C.     (2008).     Tectonic influences on the spatial and temporal  
847       evolution of the Walker Lane: An incipient transform fault along the evolving  
848       Pacific - North American plate boundary.     *Arizona Geological Society Digest*,  
849       *22*, 437–470.
- 850     Floyd, M. A., Walters, R. J., Elliott, J. R., Funning, G. J., Svarc, J. L., Murray,  
851       J. R., . . . Wright, T. J.     (2016).     Spatial variations in fault friction related  
852       to lithology from rupture and afterslip of the 2014 South Napa, Califor-  
853       nia, earthquake.     *Geophysical Research Letters*, *43*(13), 6808–6816.     doi:  
854       10.1002/2016GL069428
- 855     Fukahata, Y., & Wright, T. J.     (2008).     A non-linear geodetic data inversion using  
856       ABIC for slip distribution on a fault with an unknown dip angle.     *Geophysical*  
857       *Journal International*, *173*(2), 353–364.     doi: 10.1111/j.1365-246X.2007.03713  
858       .x
- 859     Fukuda, J.     (2018).     Variability of the Space-Time Evolution of Slow Slip Events Off  
860       the Boso Peninsula, Central Japan, From 1996 to 2014.     *Journal of Geophysical*  
861       *Research: Solid Earth*, *123*(1), 732–760. doi: 10.1002/2017JB014709

- 862 Fukuda, J., & Johnson, K. M. (2008). A fully Bayesian inversion for spatial distri-  
 863 bution of fault slip with objective smoothing. *Bulletin of the Seismological So-*  
 864 *ciety of America*, *98*(3), 1128–1146. doi: 10.1785/0120070194
- 865 Fukuda, J., & Johnson, K. M. (2010). Mixed linear-non-linear inversion of crustal  
 866 deformation data: Bayesian inference of model, weighting and regularization  
 867 parameters. *Geophysical Journal International*, *181*(3), 1441–1458. doi:  
 868 10.1111/j.1365-246X.2010.04564.x
- 869 Gavish, M., & Donoho, D. L. (2014). The optimal hard threshold for singular values  
 870 is  $4/\sqrt{3}$ . *IEEE Transactions on Information Theory*, *60*(8), 5040–5053. doi: 10  
 871 .1109/TIT.2014.2323359
- 872 Gomberg, J. (2018). Unsettled earthquake nucleation. *Nature Geoscience*, *11*(7),  
 873 463–464. doi: 10.1038/s41561-018-0149-x
- 874 Gomberg, J., & Johnson, P. (2005). Dynamic triggering of earthquakes. *Nature*,  
 875 *437*(7060), 830. doi: 10.1038/437830a
- 876 González, P. J., Samsonov, S. V., Pepe, S., Tiampo, K. F., Tizzani, P., Casu, F., ...  
 877 Sansosti, E. (2013). Magma storage and migration associated with the 2011-  
 878 2012 El Hierro eruption: Implications for crustal magmatic systems at oceanic  
 879 island volcanoes. *Journal of Geophysical Research: Solid Earth*, *118*(8), 4361–  
 880 4377. doi: 10.1002/jgrb.50289
- 881 Grandin, R., Socquet, A., Doin, M.-P., Jacques, E., de Chabalier, J.-B., & King,  
 882 G. C. P. (2010). Transient rift opening in response to multiple dike injec-  
 883 tions in the Manda Hararo rift (Afar, Ethiopia) imaged by time-dependent  
 884 elastic inversion of interferometric synthetic aperture radar data. *Journal of*  
 885 *Geophysical Research*, *115*(B9), B09403. doi: 10.1029/2009JB006883
- 886 Gualandi, A., Nichele, C., Serpelloni, E., Chiaraluce, L., Anderlini, L., Latorre, D.,  
 887 ... Avouac, J.-P. (2017). Aseismic deformation associated with an earth-  
 888 quake swarm in the northern Apennines (Italy). *Geophysical Research Letters*,  
 889 *44*(15), 7706–7714. doi: 10.1002/2017GL073687
- 890 Guglielmi, Y., Cappa, F., Avouac, J. P., Henry, P., & Elsworth, D. (2015). Seismic-  
 891 ity triggered by fluid injection-induced aseismic slip. *Science*, *348*(6240), 1224–  
 892 1226. doi: 10.1126/science.aab0476
- 893 Hamling, I. J., Hreinsdóttir, S., Clark, K., Elliott, J., Liang, C., Fielding, E.,  
 894 ... Stirling, M. (2017). Complex multifault rupture during the 2016

- 895 Mw 7.8 Kaikōura earthquake, New Zealand. *Science*, 356(6334). doi:  
896 10.1126/science.aam7194
- 897 Hammond, W. C., & Thatcher, W. (2007). Crustal deformation across the Sierra  
898 Nevada, northern Walker Lane, Basin and Range transition, western United  
899 States measured with GPS, 2000–2004. *Journal of Geophysical Research: Solid*  
900 *Earth*, 112(B5), 5411. doi: 10.1029/2006JB004625
- 901 Harris, R. A., & Segall, P. (1987). Detection of a locked zone at depth on the Park-  
902 field, California, segment of the San Andreas Fault. *Journal of Geophysical Re-*  
903 *search*, 92(B8), 7945. doi: 10.1029/JB092iB08p07945
- 904 Hatch, R. L., Abercrombie, R. E., Ruhl, C. J., & Smith, K. D. (2018). Earth-  
905 quake Interaction, Fault Structure, and Source Properties of a Small Sequence  
906 in 2017 near Truckee, CaliforniaEarthquake Interaction, Fault Structure,  
907 and Source Properties of a Small Sequence in 2017 near Truckee. *Bul-*  
908 *letin of the Seismological Society of America*, 108(5A), 2580–2593. doi:  
909 10.1785/0120180089
- 910 Hatch, R. L., Abercrombie, R. E., Ruhl, C. J., & Smith, K. D. (2020). Evidence of  
911 Aseismic and Fluid-Driven Processes in a Small Complex Seismic Swarm Near  
912 Virginia City, Nevada. *Geophysical Research Letters*, 47(4), e2019GL085477.  
913 doi: 10.1029/2019GL085477
- 914 Hatch-Ibarra, R. L., Abercrombie, R. E., Ruhl, C. J., Smith, K. D., Hammond,  
915 W. C., & Pierce, I. K. (2022). The 2016 Nine Mile Ranch Earthquakes:  
916 Hazard and Tectonic Implications of Orthogonal Conjugate Faulting in  
917 the Walker Lane. *Bulletin of the Seismological Society of America*. doi:  
918 10.1785/0120210149
- 919 Hicks, S. P., Okuwaki, R., Steinberg, A., Rychert, C. A., Harmon, N., Abercrombie,  
920 R. E., . . . Sudhaus, H. (2020). Back-propagating supershear rupture in the  
921 2016 Mw 7.1 Romanche transform fault earthquake. *Nature Geoscience*, 13(9),  
922 647–653. doi: 10.1038/s41561-020-0619-9
- 923 Hinz, N., Faulds, J., Moeck, I., Bell, J. W., & Oldow, J. S. (2010). Structural con-  
924 trols of three blind geothermal resources at the hawthorne ammunition depot,  
925 West-Central Nevada. *Transactions - Geothermal Resources Council*, 34,  
926 720–725.
- 927 Hirose, H., & Obara, K. (2010). Recurrence behavior of short-term slow slip

- 928 and correlated nonvolcanic tremor episodes in western Shikoku, southwest  
929 Japan. *Journal of Geophysical Research: Solid Earth*, 115(B6), 0–21. doi:  
930 10.1029/2008JB006050
- 931 Houston, H., Delbridge, B. G., Wech, A. G., & Creager, K. C. (2011). Rapid tremor  
932 reversals in Cascadia generated by a weakened plate interface. *Nature Geo-*  
933 *science*, 4(6), 404–409. doi: 10.1038/ngeo1157
- 934 Hussain, E., Hooper, A., Wright, T. J., Walters, R. J., & Bekaert, D. P. (2016).  
935 Interseismic strain accumulation across the central North Anatolian Fault from  
936 iteratively unwrapped InSAR measurements. *Journal of Geophysical Research:*  
937 *Solid Earth*, 121(12), 9000–9019. doi: 10.1002/2016JB013108
- 938 Ichinose, G. A., Anderson, J. G., Smith, K. D., & Zeng, Y. (2003). Source Param-  
939 eters of Eastern California and Western Nevada Earthquakes from Regional  
940 Moment Tensor Inversion. *Bulletin of the Seismological Society of America*,  
941 93(1), 61–84. doi: 10.1785/0120020063
- 942 Ingleby, T., Wright, T. J., Hooper, A., Craig, T. J., & Elliott, J. R. (2020). Con-  
943 straints on the Geometry and Frictional Properties of the Main Himalayan  
944 Thrust Using Coseismic, Postseismic, and Interseismic Deformation in Nepal.  
945 *Journal of Geophysical Research: Solid Earth*, 125(2), e2019JB019201. doi:  
946 10.1029/2019JB019201
- 947 Jiang, Y., & González, P. J. (2020). Bayesian Inversion of Wrapped Satellite  
948 Interferometric Phase to Estimate Fault and Volcano Surface Ground Defor-  
949 mation Models. *Journal of Geophysical Research: Solid Earth*, 125(5). doi:  
950 10.1029/2019JB018313
- 951 Jiang, Y., & González, P. J. (2021). High-resolution spatio-temporal fault slip using  
952 InSAR observations: insights on seismic and aseismic slip during a shallow  
953 crust earthquake swarm. In *EGU General Assembly Conference Abstracts*. doi:  
954 10.5194/egusphere-egu21-6280
- 955 Jiang, Y., González, P. J., & Bürgmann, R. (2022). Subduction earthquakes con-  
956 trolled by incoming plate geometry: The 2020  $M > 7.5$  Shumagin, Alaska,  
957 earthquake doublet. *Earth and Planetary Science Letters*, 584, 117447. doi:  
958 10.1016/J.EPSL.2022.117447
- 959 Johanson, I. A., & Bürgmann, R. (2005). Creep and quakes on the northern tran-  
960 sition zone of the San Andreas fault from GPS and InSAR data. *Geophysical*

- 961           *Research Letters*, 32(14), 1–5. doi: 10.1029/2005GL023150
- 962 Johnson, K. M., Fukuda, J., & Segall, P. (2012). Challenging the rate-state as-  
 963           perity model: Afterslip following the 2011 M9 Tohoku-oki, Japan, earth-  
 964           quake. *Geophysical Research Letters*, 39(20), 2012GL052901. doi:  
 965           10.1029/2012GL052901
- 966 Jolivet, R., Lasserre, C., Doin, M. P., Guillaso, S., Peltzer, G., Dailu, R., . . . Xu, X.  
 967           (2012). Shallow creep on the Haiyuan Fault (Gansu, China) revealed by SAR  
 968           Interferometry. *Journal of Geophysical Research: Solid Earth*, 117(B6), 6401.  
 969           doi: 10.1029/2011JB008732
- 970 Kampes, B., Hanssen, R., & Perski, Z. (2003). Radar interferometry with public do-  
 971           main tools. *Proc. of FRINGE 2003 Workshop*.
- 972 Kaneko, Y., & Shearer, P. M. (2014). Seismic source spectra and estimated stress  
 973           drop derived from cohesive-zone models of circular subshear rupture. *Geophys-  
 974           ical Journal International*, 197(2), 1002–1015. doi: 10.1093/gji/ggu030
- 975 Ke, C.-Y., McLaskey, G. C., & Kammer, D. S. (2020). The Earthquake Arrest Zone.  
 976           *Geophysical Journal International*. doi: 10.1093/gji/ggaa386
- 977 Khoshmanesh, M., Shirzaei, M., & Nadeau, R. M. (2015). Time-dependent model  
 978           of aseismic slip on the central San Andreas Fault from InSAR time series and  
 979           repeating earthquakes. *Journal of Geophysical Research: Solid Earth*, 120(9),  
 980           6658–6679. doi: 10.1002/2015JB012039
- 981 King, G. C. P., Stein, R. S., & Lin, J. (1994). Static stress changes and the trig-  
 982           gering of earthquakes. *Bulletin of the Seismological Society of America*, 84(3),  
 983           935–953.
- 984 Klein, E., Duputel, Z., Zigone, D., Vigny, C., Boy, J.-P., Doubre, C., & Meneses,  
 985           G. (2018). Deep transient slow slip detected by survey gps in the region of  
 986           atacama, chile. *Geophysical Research Letters*, 45(22), 12,263–12,273. doi:  
 987           10.1029/2018GL080613
- 988 Kreemer, C., Blewitt, G., & Hammond, W. C. (2009). Geodetic constraints on  
 989           contemporary deformation in the northern Walker Lane: 2. Velocity and  
 990           strain rate tensor analysis. In *Late Cenozoic Structure and Evolution of the  
 991           Great Basin-Sierra Nevada Transition*. Geological Society of America. doi:  
 992           10.1130/2009.2447(02)
- 993 Kreemer, C., Blewitt, G., & Klein, E. C. (2014). A geodetic plate motion and Global

- 994 Strain Rate Model. *Geochemistry, Geophysics, Geosystems*, 15(10), 3849–3889.  
 995 doi: 10.1002/2014GC005407
- 996 Kyriakopoulos, C., Chini, M., Bignami, C., Stramondo, S., Ganas, A., Kolligri, M.,  
 997 & Moshou, A. (2013). Monthly migration of a tectonic seismic swarm detected  
 998 by DInSAR: Southwest Peloponnese, Greece. *Geophysical Journal Interna-*  
 999 *tional*, 194(3), 1302–1309. doi: 10.1093/gji/ggt196
- 1000 Lambert, V., Lapusta, N., & Perry, S. (2021). Propagation of large earthquakes as  
 1001 self-healing pulses or mild cracks. *Nature*, 591(7849), 252–258. doi: 10.1038/  
 1002 s41586-021-03248-1
- 1003 Lange, R. A., & Carmichael, I. S. E. (1996). The Aurora volcanic field, California-  
 1004 Nevada: oxygen fugacity constraints on the development of andesitic  
 1005 magma. *Contributions to Mineralogy and Petrology*, 125(2), 167–185. doi:  
 1006 10.1007/s004100050214
- 1007 Liu, Y., McGuire, J. J., & Behn, M. D. (2020). Aseismic transient slip on the Go-  
 1008 far transform fault, East Pacific Rise. *Proceedings of the National Academy of*  
 1009 *Sciences of the United States of America*, 117(19), 10188–10194. doi: 10.1073/  
 1010 pnas.1913625117
- 1011 Lohman, R. B., & McGuire, J. J. (2007). Earthquake swarms driven by aseismic  
 1012 creep in the Salton Trough, California. *Journal of Geophysical Research: Solid*  
 1013 *Earth*, 112(4). doi: 10.1029/2006JB004596
- 1014 Luo, Y., & Liu, Z. (2019). Rate-and-State Model Casts New Insight into Episodic  
 1015 Tremor and Slow-slip Variability in Cascadia. *Geophysical Research Letters*,  
 1016 46(12), 6352–6362. doi: 10.1029/2019GL082694
- 1017 Madariaga, R. (1976). Dynamics of an expanding circular fault. *Bulletin of the Seis-*  
 1018 *mological Society of America*, 66(3), 639–666.
- 1019 Mai, P. M., & Beroza, G. C. (2002). A spatial random field model to characterize  
 1020 complexity in earthquake slip. *Journal of Geophysical Research: Solid Earth*,  
 1021 107(B11), ESE 10–1–ESE 10–21. doi: 10.1029/2001jb000588
- 1022 Mai, P. M., & Thingbaijam, K. K. (2014). SRCMOD: An online database of finite-  
 1023 fault rupture models. *Seismological Research Letters*, 85(6), 1348–1357. doi:  
 1024 10.1785/0220140077
- 1025 Marone, C., & Richardson, E. (2006). Do earthquakes rupture piece by piece or all  
 1026 together? *Science*, 313(5794), 1748–1749. doi: 10.1126/science.1131296

- 1027 Matthews, M. V., & Segall, P. (1993). Estimation of depth-dependent fault slip  
 1028 from measured surface deformation with application to the 1906 San Francisco  
 1029 earthquake. *Journal of Geophysical Research*, *98*(B7), 12153–12163. doi:  
 1030 10.1029/93jb00440
- 1031 Mesimeri, M., & Karakostas, V. (2018). Repeating earthquakes in western Corinth  
 1032 Gulf (Greece): Implications for aseismic slip near locked faults. *Geophysical*  
 1033 *Journal International*, *215*(1), 659–676. doi: 10.1093/gji/ggy301
- 1034 Michel, S., Gualandi, A., & Avouac, J. P. (2019). Similar scaling laws for earth-  
 1035 quakes and Cascadia slow-slip events. *Nature*, *574*(7779), 522–526. doi: 10  
 1036 .1038/s41586-019-1673-6
- 1037 Minson, S. E., Simons, M., & Beck, J. L. (2013). Bayesian inversion for finite fault  
 1038 earthquake source models I—theory and algorithm. *Geophysical Journal Inter-*  
 1039 *national*, *194*(3), 1701–1726. doi: 10.1093/gji/ggt180
- 1040 Mori, J. (1996). Rupture directivity and slip distribution of the M 4.3 foreshock to  
 1041 the 1992 Joshua Tree earthquake, Southern California. *Bulletin of the Seismo-*  
 1042 *logical Society of America*, *86*(3), 805–810. doi: 10.1785/BSSA0860030805
- 1043 Nadeau, R. M., & McEvilly, T. V. (1999). Fault slip rates at depth from recurrence  
 1044 intervals of repeating microearthquakes. *Science*, *285*(5428), 718–721. doi: 10  
 1045 .1126/science.285.5428.718
- 1046 Nissen, E., Ghorashi, M., Jackson, J., Parsons, B., & Talebian, M. (2007). The  
 1047 2005 Qeshm Island earthquake (Iran) - A link between buried reverse faulting  
 1048 and surface folding in the Zagros Simply Folded Belt? *Geophysical Journal*  
 1049 *International*, *171*(1), 326–338. doi: 10.1111/j.1365-246X.2007.03514.x
- 1050 Ozawa, S., Yarai, H., & Kobayashi, T. (2019). Recovery of the recurrence interval of  
 1051 Boso slow slip events in Japan. *Earth, Planets and Space*, *71*(1), 1–8. doi: 10  
 1052 .1186/s40623-019-1058-y
- 1053 Parotidis, M., Rothert, E., & Shapiro, S. A. (2003). Pore-pressure diffu-  
 1054 sion: A possible triggering mechanism for the earthquake swarms 2000 in  
 1055 Vogtland/NW-Bohemia, central Europe. *Geophysical Research Letters*, *30*(20),  
 1056 2003GL018110. doi: 10.1029/2003GL018110
- 1057 Passarelli, L., Rivalta, E., Jónsson, S., Hensch, M., Metzger, S., Jakobsdóttir, S. S.,  
 1058 ... Dahm, T. (2018). Scaling and spatial complementarity of tectonic  
 1059 earthquake swarms. *Earth and Planetary Science Letters*, *482*, 62–70. doi:

- 1060 10.1016/j.epsl.2017.10.052
- 1061 Pritchard, M. E., & Simons, M. (2006). An aseismic slip pulse in northern Chile  
1062 and along-strike variations in seismogenic behavior. *Journal of Geophysical Re-*  
1063 *search: Solid Earth*, 111(8). doi: 10.1029/2006JB004258
- 1064 Radiguet, M., Cotton, F., Vergnolle, M., Campillo, M., Valette, B., Kostoglodov, V.,  
1065 & Cotte, N. (2011). Spatial and temporal evolution of a long term slow slip  
1066 event: the 2006 Guerrero Slow Slip Event. *Geophysical Journal International*,  
1067 184(2), 816–828. doi: 10.1111/j.1365-246X.2010.04866.x
- 1068 Radiguet, M., Perfettini, H., Cotte, N., Gualandi, A., Valette, B., Kostoglodov, V.,  
1069 ... Campillo, M. (2016). Triggering of the 2014 Mw7.3 Papanoa earthquake  
1070 by a slow slip event in Guerrero, Mexico. *Nature Geoscience* 2016 9:11, 9(11),  
1071 829–833. doi: 10.1038/ngeo2817
- 1072 Ragon, T., Sladen, A., & Simons, M. (2018). Accounting for uncertain fault geome-  
1073 try in earthquake source inversions – I: theory and simplified application. *Geo-*  
1074 *physical Journal International*, 214(2), 1174–1190. doi: 10.1093/gji/ggy187
- 1075 Romanet, P., Bhat, H. S., Jolivet, R., & Madariaga, R. (2018). Fast and Slow Slip  
1076 Events Emerge Due to Fault Geometrical Complexity. *Geophysical Research*  
1077 *Letters*, 45(10), 4809–4819. doi: 10.1029/2018GL077579
- 1078 Rousset, B., Fu, Y., Bartlow, N., & Bürgmann, R. (2019). Weeks-Long and Years-  
1079 Long Slow Slip and Tectonic Tremor Episodes on the South Central Alaska  
1080 Megathrust. *Journal of Geophysical Research: Solid Earth*, 124(12), 13392–  
1081 13403. doi: 10.1029/2019JB018724
- 1082 Ruhl, C. J., Abercrombie, R. E., Smith, K. D., & Zaliapin, I. (2016). Complex  
1083 spatiotemporal evolution of the 2008 Mw 4.9 Mogul earthquake swarm (Reno,  
1084 Nevada): Interplay of fluid and faulting. *Journal of Geophysical Research:*  
1085 *Solid Earth*, 121(11), 8196–8216. doi: 10.1002/2016JB013399
- 1086 Ruhl, C. J., Morton, E. A., Bormann, J. M., Hatch-Ibarra, R., Ichinose, G., &  
1087 Smith, K. D. (2021). Complex Fault Geometry of the 2020 Mww 6.5 Monte  
1088 Cristo Range, Nevada, Earthquake Sequence. *Seismological Research Letters*,  
1089 92, 1876-1890. doi: 10.1785/0220200345
- 1090 Salman, R., Hill, E. M., Feng, L., Lindsey, E. O., Mele Veedu, D., Barbot, S., ...  
1091 Natawidjaja, D. H. (2017). Piecemeal Rupture of the Mentawai Patch, Suma-  
1092 tra: The 2008 Mw 7.2 North Pagai Earthquake Sequence. *Journal of Geophys-*

- 1093            *ical Research: Solid Earth*, 122(11), 9404–9419. doi: 10.1002/2017JB014341
- 1094 Samsonov, S., & D’Oreye, N.    (2012).    Multidimensional time-series analysis of
- 1095            ground deformation from multiple InSAR data sets applied to Virunga Vol-
- 1096            canic Province.    *Geophysical Journal International*, 191(3), 1095–1108.    doi:
- 1097            10.1111/j.1365-246X.2012.05669.x
- 1098 Schmidt, D. A., Bürgmann, R., Nadeau, R. M., & D’Alessio, M. (2005). Distribution
- 1099            of aseismic slip rate on the Hayward fault inferred from seismic and geode-
- 1100            tic data.    *Journal of Geophysical Research: Solid Earth*, 110(B8), 1–15.    doi:
- 1101            10.1029/2004JB003397
- 1102 Scott, C., Bunds, M., Shirzaei, M., & Toke, N. (2020). Creep Along the Central San
- 1103            Andreas Fault From Surface Fractures, Topographic Differencing, and InSAR.
- 1104            *Journal of Geophysical Research: Solid Earth*, 125(10), e2020JB019762.    doi:
- 1105            10.1029/2020JB019762
- 1106 Segall, P., & Rice, J. R.    (1995).    Dilatancy, compaction, and slip instability of a
- 1107            fluid-infiltrated fault.    *Journal of Geophysical Research: Solid Earth*, 100(B11),
- 1108            22155–22171. doi: 10.1029/95JB02403
- 1109 Segall, P., Rubin, A. M., Bradley, A. M., & Rice, J. R.    (2010).    Dilatant strength-
- 1110            ening as a mechanism for slow slip events.    *Journal of Geophysical Research*,
- 1111            115(B12), B12305. doi: 10.1029/2010JB007449
- 1112 Shearer, P. M., Prieto, G. A., & Hauksson, E.    (2006).    Comprehensive analysis of
- 1113            earthquake source spectra in southern California.    *Journal of Geophysical Re-*
- 1114            *search: Solid Earth*, 111(B6), 6303. doi: 10.1029/2005JB003979
- 1115 Shen, Z. K., Sun, J., Zhang, P., Wan, Y., Wang, M., Bürgmann, R., . . . Wang,
- 1116            Q.    (2009).    Slip maxima at fault junctions and rupturing of barriers during
- 1117            the 2008 Wenchuan earthquake.    *Nature Geoscience*, 2(10), 718–724.    doi:
- 1118            10.1038/ngeo636
- 1119 Smith, K., Johnson, C., Davies, J., Agbaje, T., Knezevic Antonijevic, S., & Kent, G.
- 1120            (2011).    The 2011 Hawthorne, Nevada, Earthquake Sequence: Shallow Normal
- 1121            Faulting. In *AGU Fall Meeting* (pp. S53B–2284).
- 1122 Song, X., Jiang, Y., Shan, X., Gong, W., & Qu, C.    (2019).    A Fine Velocity and
- 1123            Strain Rate Field of Present-Day Crustal Motion of the Northeastern Tibetan
- 1124            Plateau Inverted Jointly by InSAR and GPS.    *Remote Sensing 2019, Vol. 11,*
- 1125            *Page 435*, 11(4), 435. doi: 10.3390/RS11040435

- 1126 Stein, S., & Gordon, R. G. (1984). Statistical tests of additional plate boundaries  
 1127 from plate motion inversions. *Earth and Planetary Science Letters*, *69*(2), 401–  
 1128 412. doi: 10.1016/0012-821X(84)90198-5
- 1129 Sun, J., Johnson, K. M., Cao, Z., Shen, Z., Bürgmann, R., & Xu, X. (2011). Me-  
 1130chanical constraints on inversion of coseismic geodetic data for fault slip and  
 1131 geometry: Example from InSAR observation of the 6 October 2008 Mw 6.3  
 1132 Dangxiong-Yangyi (Tibet) earthquake. *Journal of Geophysical Research*,  
 1133 *116*(B1), B01406. doi: 10.1029/2010JB007849
- 1134 Takenaka, H., & Fujii, Y. (2008). A compact representation of spatio-temporal slip  
 1135 distribution on a rupturing fault. *Journal of Seismology*, *12*, 281–293. doi: 10  
 1136 .1007/s10950-007-9087-6
- 1137 Taymaz, T., Wright, T. J., Yolsal, S., Tan, O., Fielding, E., & Seyitoğlu, G. (2007).  
 1138 Source characteristics of the 6 June 2000 Orta-Çankiri (central Turkey) earth-  
 1139 quake: A synthesis of seismological, geological and geodetic (InSAR) obser-  
 1140 vations, and internal deformation of the Anatolian plate. *Geological Society*  
 1141 *Special Publication*, *291*(1), 259–290. doi: 10.1144/SP291.12
- 1142 Thatcher, W., Foulger, G. R., Julian, B. R., Svarc, J., Quilty, E., & Bawden,  
 1143 G. W. (1999, 3). Present-day deformation across the basin and range  
 1144 province, western united states. *Science*, *283*, 1714–1718. doi: 10.1126/  
 1145 SCIENCE.283.5408.1714
- 1146 Thomas, M. Y., Avouac, J.-P., Champenois, J., Lee, J.-C., Kuo, L.-C., Thomas,  
 1147 M. Y., ... Kuo, L.-C. (2014). Spatiotemporal evolution of seismic and aseis-  
 1148 mic slip on the Longitudinal Valley Fault, Taiwan. *Journal of Geophysical*  
 1149 *Research: Solid Earth*, *119*(6), 5114–5139. doi: 10.1002/2013JB010603
- 1150 Tridon, M., Cayol, V., Froger, J., Augier, A., & Bachèlery, P. (2016). Inversion of co-  
 1151 eval shear and normal stress of Piton de la Fournaise flank displacement. *Jour-  
 1152 nal of Geophysical Research: Solid Earth*, *121*(11), 7846–7866. doi: 10.1002/  
 1153 2016JB013330
- 1154 Tsang, L. L. H., Hill, E. M., Barbot, S., Qiu, Q., Feng, L., Hermawan, I., ... Nataw-  
 1155 idjaja, D. H. (2016). Afterslip following the 2007 Mw 8.4 Bengkulu earthquake  
 1156 in Sumatra loaded the 2010 Mw 7.8 Mentawai tsunami earthquake rupture  
 1157 zone. *Journal of Geophysical Research: Solid Earth*, *121*(12), 9034–9049. doi:  
 1158 10.1002/2016JB013432

- 1159 Turner, R. C., Nadeau, R. M., & Bürgmann, R. (2013). Aseismic slip and fault in-  
 1160 teraction from repeating earthquakes in the Loma Prieta aftershock zone. *Geo-*  
 1161 *physical Research Letters*, *40*(6), 1079–1083. doi: 10.1002/grl.50212
- 1162 Uchide, T., Shearer, P. M., & Imanishi, K. (2014). Stress drop variations among  
 1163 small earthquakes before the 2011 Tohoku-oki, Japan, earthquake and impli-  
 1164 cations for the main shock. *Journal of Geophysical Research: Solid Earth*,  
 1165 *119*(9), 7164–7174. doi: 10.1002/2014JB010943
- 1166 Villegas-Lanza, J. C., Nocquet, J. M., Rolandone, F., Vallee, M., Tavera, H., Bon-  
 1167 doux, F., . . . Chlieh, M. (2016). A mixed seismic-aseismic stress release  
 1168 episode in the Andean subduction zone. *Nature Geoscience*, *9*(2), 150–154.  
 1169 doi: 10.1038/ngeo2620
- 1170 Wallace, L. M. (2020). Slow Slip Events in New Zealand. *Annual Review of Earth*  
 1171 *and Planetary Sciences*, *48*(1), 175–203. doi: 10.1146/annurev-earth-071719  
 1172 -055104
- 1173 Wallace, L. M., Beavan, J., Bannister, S., & Williams, C. (2012). Simultaneous long-  
 1174 term and short-term slow slip events at the Hikurangi subduction margin, New  
 1175 Zealand: Implications for processes that control slow slip event occurrence,  
 1176 duration, and migration. *Journal of Geophysical Research B: Solid Earth*,  
 1177 *117*(11). doi: 10.1029/2012JB009489
- 1178 Walters, R. J., Elliott, J. R., D’Agostino, N., England, P. C., Hunstad, I., Jackson,  
 1179 J. A., . . . Roberts Edinburgh, G. (2009). The 2009 L’Aquila earthquake  
 1180 (central Italy): A source mechanism and implications for seismic hazard. *Geo-*  
 1181 *physical Research Letters*, *36*(17). doi: 10.1029/2009GL039337
- 1182 Wech, A. G., Creager, K. C., & Melbourne, T. I. (2009). Seismic and geodetic con-  
 1183 straints on Cascadia slow slip. *Journal of Geophysical Research: Solid Earth*,  
 1184 *114*(10). doi: 10.1029/2008JB006090
- 1185 Werner, C. (2000). GAMMA SAR and interferometric processing software. *Proceed-*  
 1186 *ings of ERS-Envisat Symposium ; 16-20 October, Gothenburg, Sweden, 2000*.
- 1187 Wesnousky, S. (2005). Active faulting in the Walker Lane. *Tectonics*, *24*(3). doi: 10  
 1188 .1029/2004TC001645
- 1189 Wicks, C., Thelen, W., Weaver, C., Gomberg, J., Rohay, A., & Bodin, P. (2011).  
 1190 InSAR observations of aseismic slip associated with an earthquake swarm in  
 1191 the Columbia River flood basalts. *Journal of Geophysical Research*, *116*(B12),

- 1192 B12304. doi: 10.1029/2011JB008433
- 1193 Xu, W., Bürgmann, R., & Li, Z. (2016). An improved geodetic source model for the  
1194 1999 Mw 6.3 Chamoli earthquake, India. *Geophysical Journal International*,  
1195 *205*(1), 236–242. doi: 10.1093/gji/ggw016
- 1196 Yamashita, Y., Yakiwara, H., Asano, Y., Shimizu, H., Uchida, K., Hirano, S., ...  
1197 Obara, K. (2015). Migrating tremor off southern Kyushu as evidence for  
1198 slow slip of a shallow subduction interface. *Science*, *348*(6235), 676–679. doi:  
1199 10.1126/science.aaa4242
- 1200 Zha, X., Jia, Z., Dai, Z., & Lu, Z. (2019). The cause of the 2011 Hawthorne  
1201 (Nevada) earthquake swarm constrained by seismic and InSAR methods.  
1202 *Journal of Geodesy*, *93*(6), 899–909. doi: 10.1007/s00190-018-1212-5

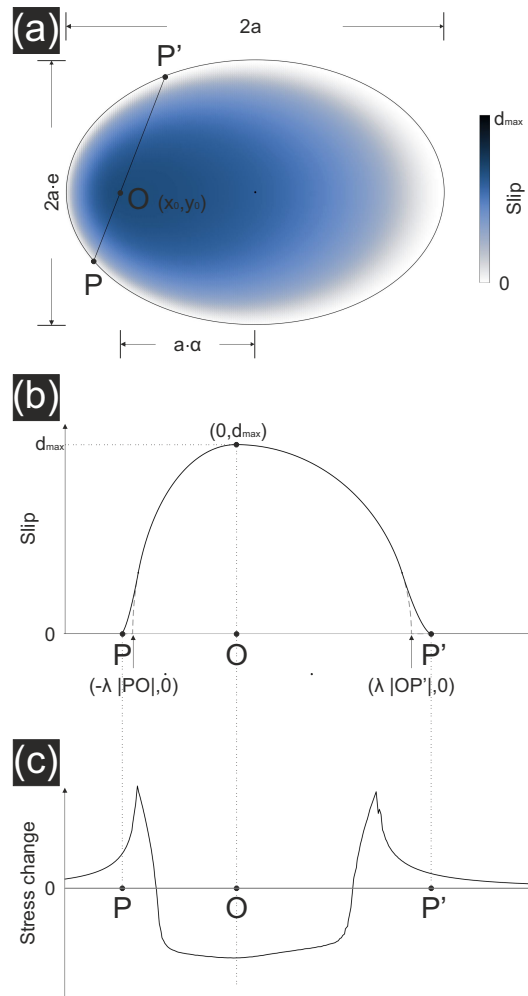


**Figure 1.** Parameters of the proposed slip model. Image (a) shows the 2d slip distribution, with an elliptical shape. The slip and stress changes along profile POP' are presented in images (b)-(c).

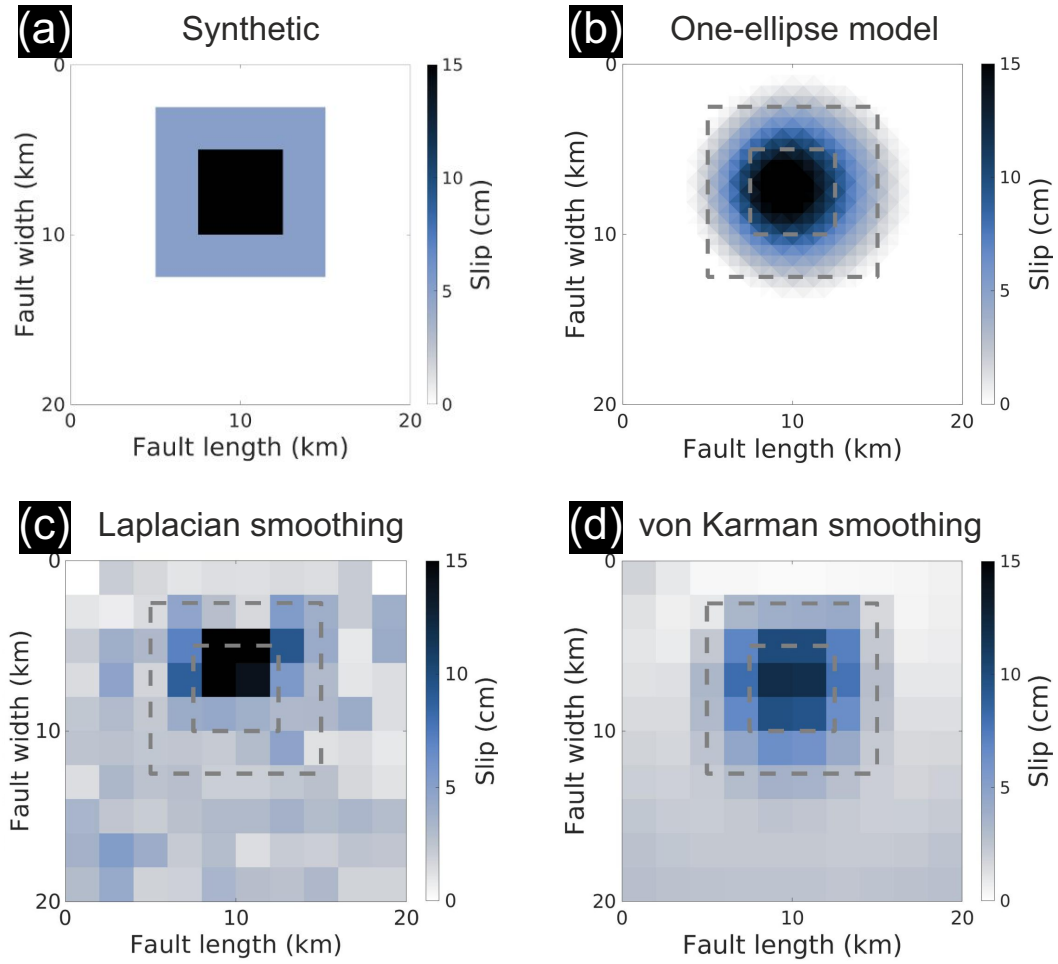


**Figure 2.** Synthetic and modelled fault slip distribution for a synthetic case. Image (a) shows the synthetic non-uniform slip distribution on a simulated fault plane. The black area is a 5 km  $\times$  5 km region with 15 cm down-dip slip. The blue area is a 10 km  $\times$  10 km region with 5 cm down-dip slip. No slip occurs in the white area. Images (b)-(d) are the inverted fault slip distribution based on the optimal model with maximum likelihood estimated by the one-ellipse model (GICMo), the Laplacian smoothing and the von Karman smoothing (slipBERI). The dashed line in image (b)-(d) indicate the boundary of various slipping area in image (a).

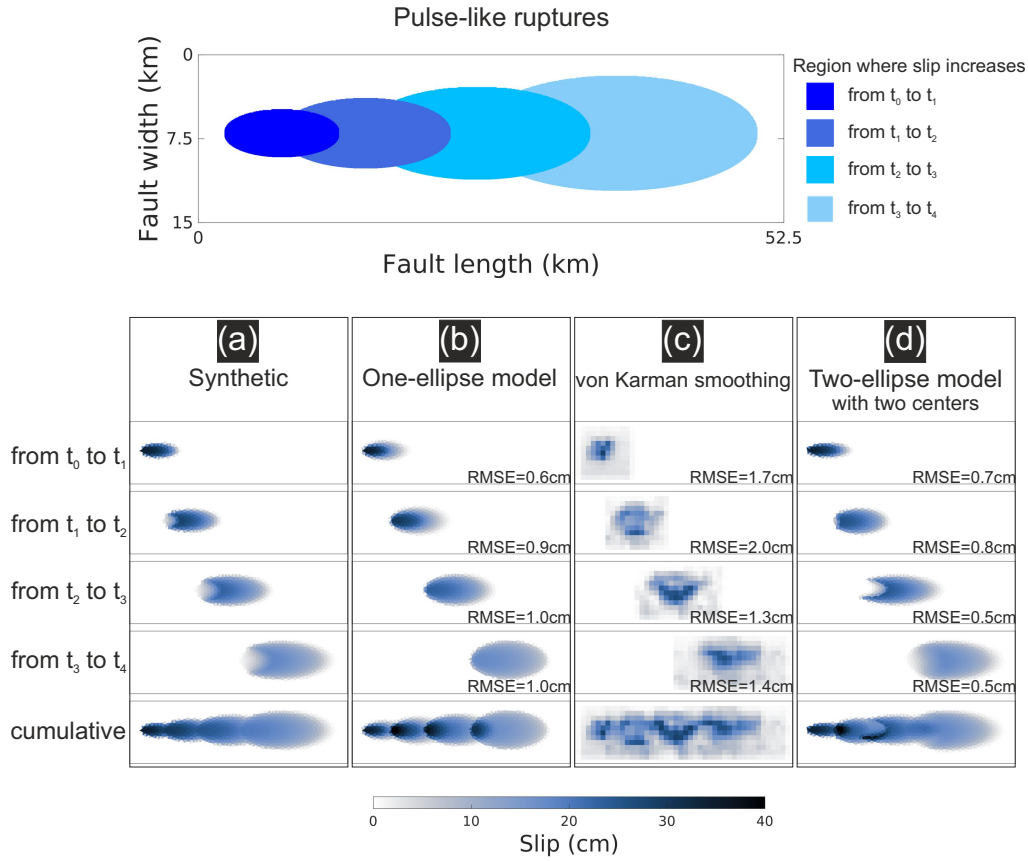


**Figure 3.** Synthetic and modelled fault slip distributions for synthetic case 2 (pulse-like ruptures). The top image is the conceptual diagram representing the growing cracks with the overlapping relationship. Images in column (a) show the synthetic slip increments. Images in columns (b)-(d) show the modelled slip distribution with various inversion methods: the one-ellipse model (b), the von Karman smoothing (c), and the two-ellipse model with different centres (d), and the RMSE of the slip residuals are shown at the bottom right.

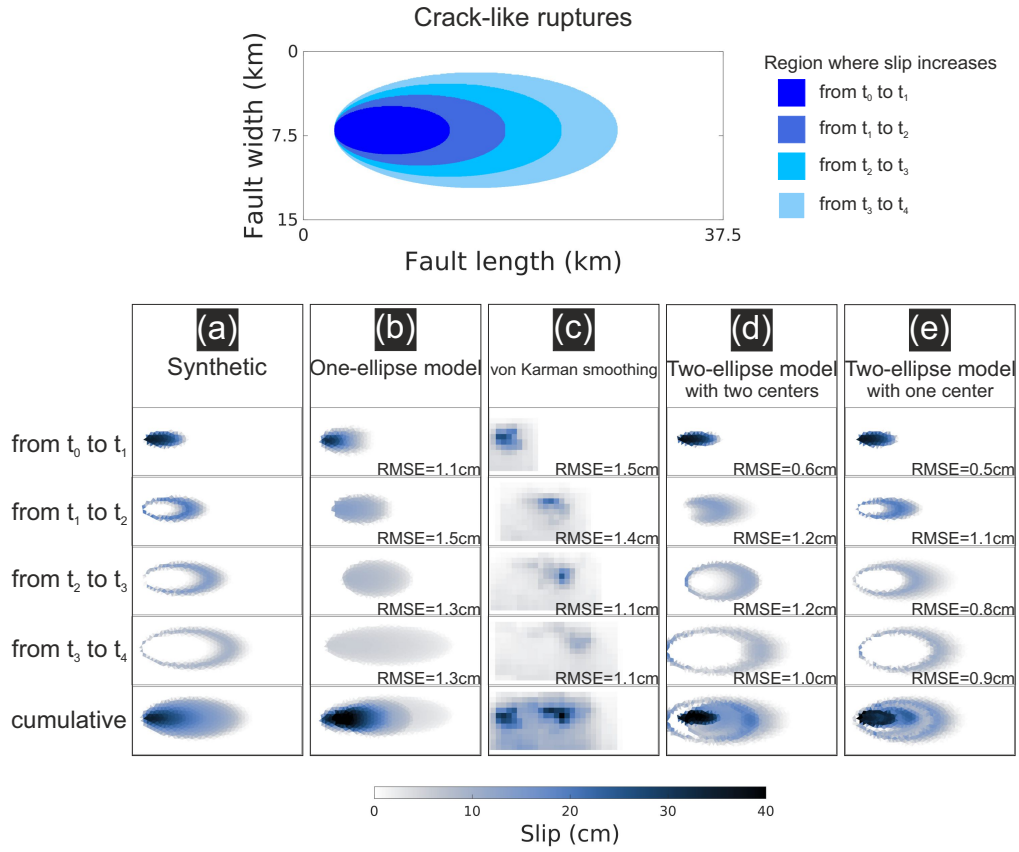


**Figure 4.** Synthetic and modelled fault slip distribution for synthetic case 2 (crack-like ruptures). The top image is the conceptual diagram presenting the growing cracks with the containing relationship. Images in column (a) show the synthetic slip increments. Images in columns (b)-(e) show the modelled slip distribution with various inversion methods: the one-ellipse model (b), the von Karman smoothing (c), the two-ellipse model with different centres (d) and with the same centre (e), and the RMSE of the slip residuals are shown at the bottom right.

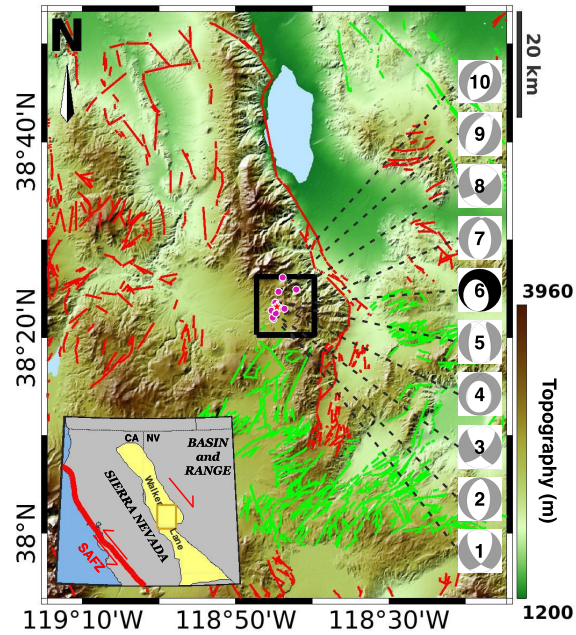


**Figure 5.** Tectonic settings for the 2011 Hawthorne seismic swarm. Image (a) shows the structural geologic environment of Walker Lane, located between the Sierra Nevada microplate and Basin and Range Province. It accommodates relative motion between the Pacific and North America. The brown rectangular box is the boundary of image (b), the central segment of Walker Lane. Image (b) shows the detailed tectonic settings for the 2011 Hawthorne seismic swarm, with topography as the base map. Normal and strike-slip faults are plotted as red and green lines. The beach balls on the right show the focal mechanism solutions provided by the Nevada Seismological Laboratory (Ichinose et al., 2003). Beach ball No.6 in black is the event with the largest magnitude, M4.6. Abbreviation: SAFZ, San Andreas Fault Zone.

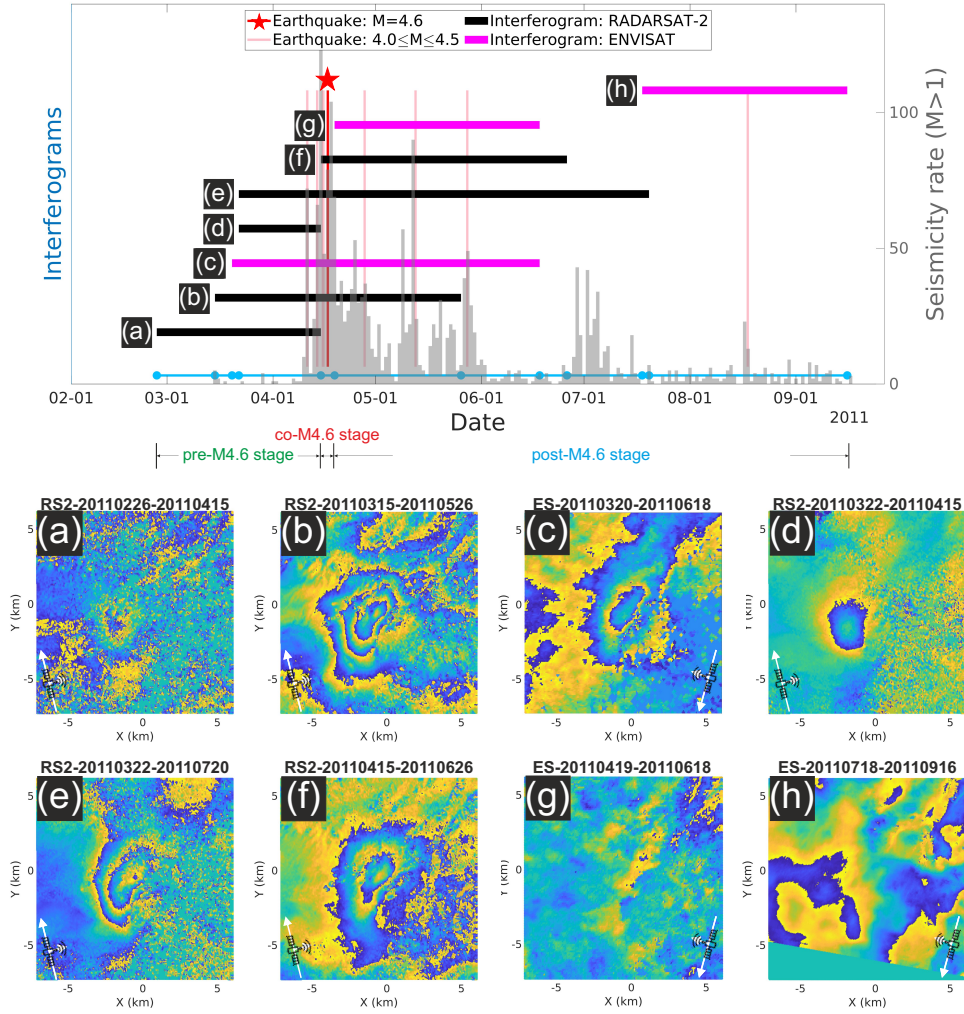


**Figure 6.** Surface displacement observations for the 2011 Hawthorne seismic swarm. In this research, the 2011 Hawthorne seismic swarm is divided into 3 stages with respect to the largest event, M4.6 on April 17 2011 (red star in the top image): pre-, co- and post-M4.6 event. The top image shows the time coverage of the interferograms (horizontal lines) over  $M \geq 4$  events (vertical lines). Out of 8 interferograms (a)-(h), 5 are from RADARSAT-2 (black lines) and 3 from ENVISAT (magenta lines). For the blue line at the bottom, dots infer the 11 dates for the image sensing time in the interferograms. Images (a)-(g) show the observed wrapped phases of the interferograms capturing the surface deformation of the seismic swarm, while no clear deformation signal is detectable in image (h). The spatial reference point is [38.3875°N, 118.725°W].

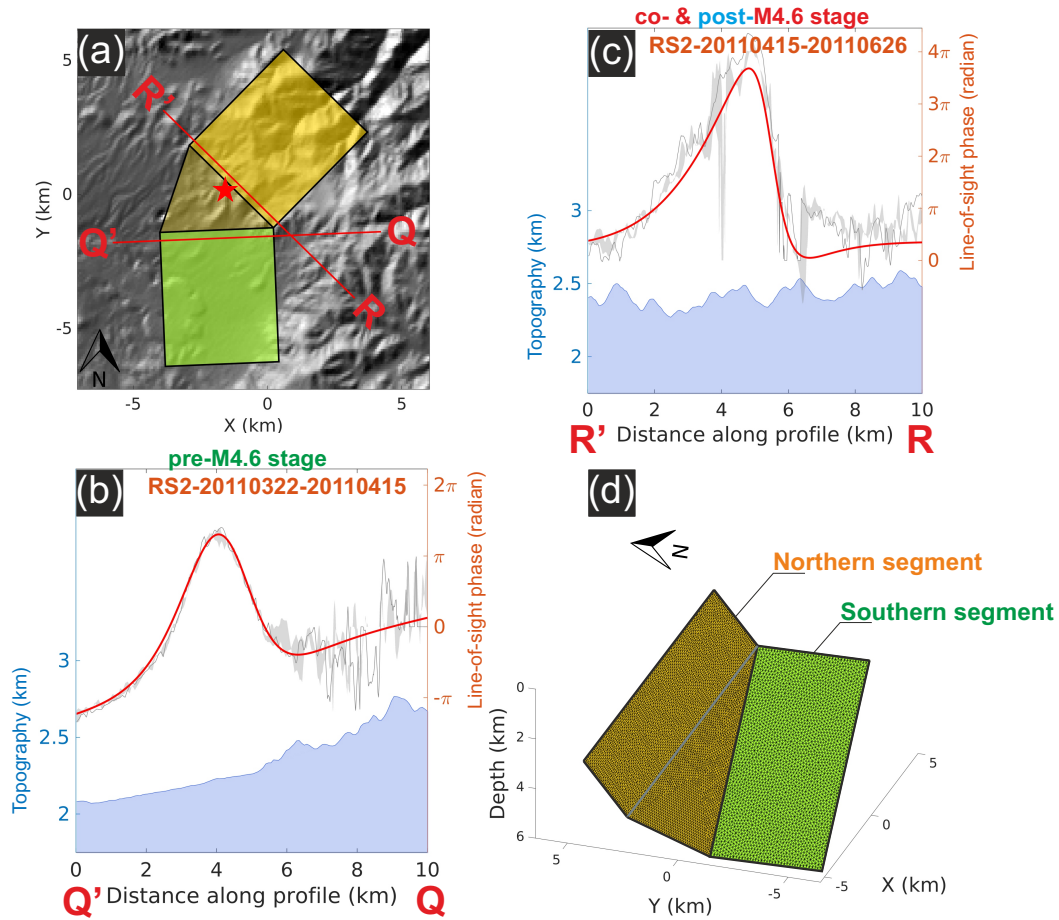


**Figure 7.** Fault geometry for the 2011 Hawthorne seismic swarm. Image (a) indicates the fault plane with uniform slip retrieved by WGBIS (Jiang & González, 2020) from the wrapped interferograms, and the modelled phase and phase residuals are shown in Figure S8. In image (a), the green rectangle indicates the southern subfault which is active during the pre-M4.6 stage, retrieved from RADARSAT-2 interferogram 2011/03/22-2011/04/15; yellow rectangle indicates the northern subfault which is active during the co- and post-M4.6 stages, retrieved from the RADARSAT-2 interferogram 2011/04/15-2011/06/26, and the yellow triangle indicates the joint fault connecting two rectangle subfaults. Profiles QQ' and RR' are perpendicular to two rectangle subfaults and the red star indicates the hypocentre of the M4.6 event. Images (b) and (c) show the observed and modelled phase along profiles QQ' and RR'. Image (d) shows the discretization of the fault geometry in image (a), where the triangular mesh is generated by FaultResampler (Barnhart & Lohman, 2010) and mesh2d (Engwirda, 2014).

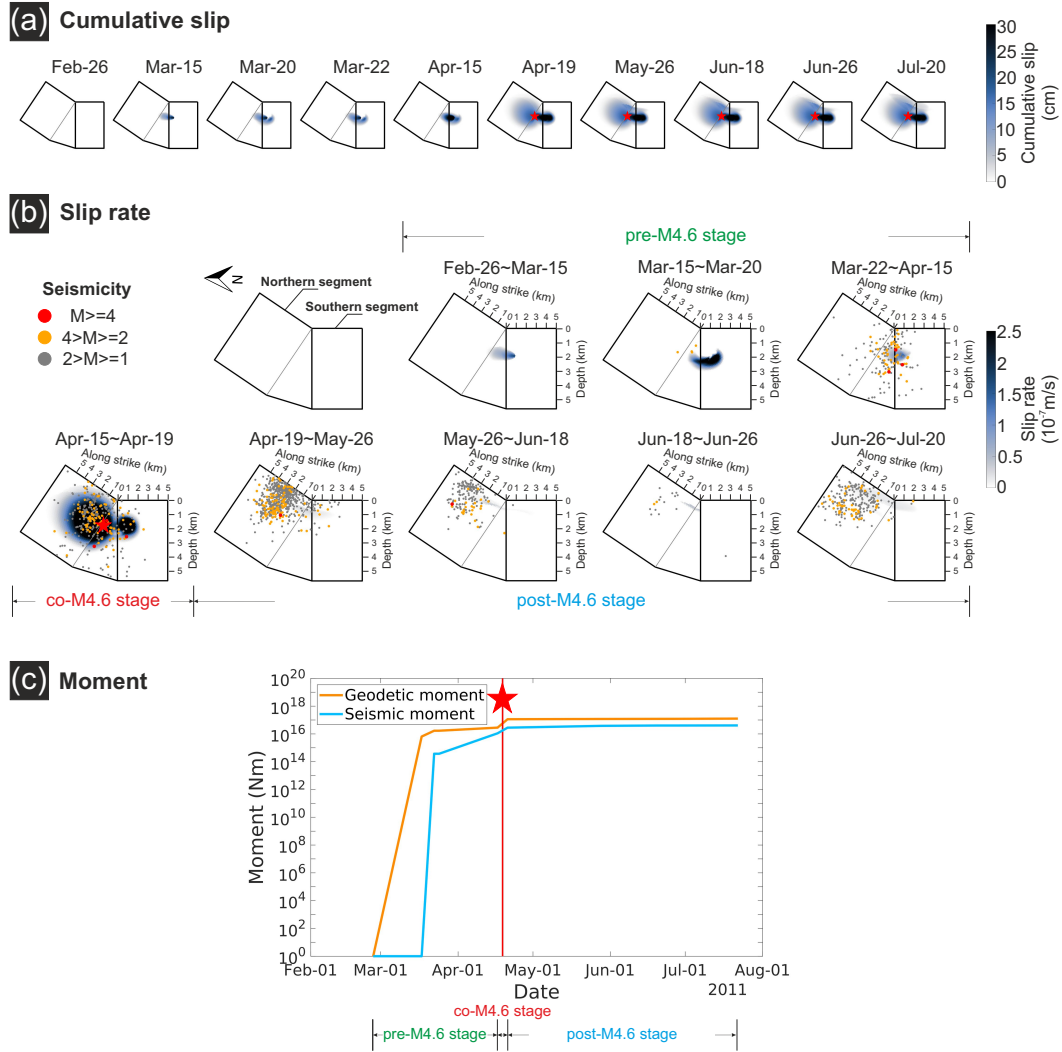


**Figure 8.** Slip evolution obtained from Time-GICMo inversion of pre-, co- and post-M4.6 stages during 2011 Hawthorne seismic swarm. Image (a) shows the accumulated slip at 10 dates, representing the acquisition time of images in Figures 6a to 6g. Image (b) presents the slip rate during the pre-, co- and post-M4.6 stages. In image (c), blue line shows the cumulative seismic moment based on the USGS earthquake catalog in the region [ $38.325^{\circ}\text{N} \sim 38.45^{\circ}\text{N}$ ,  $118.675^{\circ}\text{W} \sim 118.775^{\circ}\text{W}$ ] (<https://earthquake.usgs.gov/earthquakes/search/>); orange line shows the cumulative geodetic moment, on the basis of estimated cumulative slip in image (a). A variable crustal shear modulus with depth is assumed based on the CRUST 1.0 model in the moment calculation.